VIBRATION-BASED PIEZOELECTRIC ENERGY HARVESTING SYSTEM FOR ROTARY MOTION APPLICATIONS

by

Farbod Khameneifar
B.Sc. in Mechanical Engineering, University of Tehran, 2008

THESIS SUBMITTED IN PARTIAL FULFILLMENT OF
THE REQUIREMENTS FOR THE DEGREE OF

MASTER OF APPLIED SCIENCE

In the
Mechatronic Systems Engineering, School of Engineering Science

SIMON FRASER UNIVERSITY

Spring 2011

APPROVAL

Name: **Farbod Khameneifar**

Degree: **Master of Applied Science**

Title of Thesis: **Vibration-based Piezoelectric Energy Harvesting System for Rotary Motion Applications**

Examining Committee:

Chair: **Dr. G. Wang**
Associate Professor of Engineering Science

Senior Joint Supervisors:

Dr. S. Arzanpour
Assistant Professor of Engineering Science

Dr. M. Moallem
Associate Professor of Engineering Science

Supervisor:

Dr. E. Park
Associate Professor of Engineering Science

Internal Examiner:

Dr. W. Kim
Assistant Professor of Engineering Science

Date Defended/Approved: April-04-2011

Declaration of
Partial Copyright Licence

ABSTRACT

The modelling and design of a piezoelectric mounted rotary flexible beam that can be used as an energy scavenger for rotary motion applications is investigated in this thesis. The energy harvester system consists of a piezoelectric cantilever beam with a tip mass mounted on a rotating hub. Development of the energy harvester is motivated by the need to continuously charge wireless sensors for health (condition) monitoring in rotating mechanisms such as tires and turbines. A review of prior energy harvester mechanisms is provided followed by the proposed design and modelling technique. The dynamic model of the harvester is derived by using the Euler-Bernoulli beam equation and considering the effect of the piezoelectric transducer. The equations of motion are derived using the Lagrangian approach followed by relationships describing the harvested power. In particular, expressions describing the optimum load resistance and the maximum power that can be harvested using the proposed system are derived. Numerical simulations are performed to show the performance of the harvester by obtaining tip velocities and electrical output voltages for a range of electrical load resistances and rotational speeds. Effect of parameters such as tip mass weight, beam length, piezoelectric constant, compliance, relative permittivity and damping on the harvester dynamics analyzed. Design and fabrication of the prototype are presented further. The model is verified for resonance and off-resonance operation by comparison to the experimental results. It is shown that by proper sizing and parameter selection the output power of the proposed system is sufficient to power typical wireless sensors.

Keywords: Piezoelectric Energy harvester, Flexible cantilever dynamics, Rotary motion instrumentation.

ACKNOWLEDGEMENTS

I owe my deepest gratitude to everyone that helped accomplish this work. First to my supervisors, Dr. Siamak Arzanpour and Dr. Mehrdad Moallem, who have been true colleagues in this endeavor: thank you for your guidance, support and patience. I learnt many things that I will carry with me for the rest of my life. I wish you all the best in future.

Next, I want to thank all of my lab mates. Thanks to all for the support and advice. The times we spent together in the lab have been priceless.

Last, but most importantly, my appreciation to my family, my parents for their support and love through the years and my sister for her encouragement.

TABLE OF CONTENTS

LIST OF FIGURES

LIST OF TABLES

CHAPTER 1: INTRODUCTION

Rotation is one of the most commonly used forms of mechanical motion and power transmission, widely used in various platforms in engineering applications. Apart from the design and manufacturing issues, maintenance and condition monitoring of rotary systems are of great importance in different applications. For instance, a gas turbine power generation unit cannot be shut down instantly for checkups or inspection purposes. Instead, it is desirable to continuously monitor the health and status of the system while it is operating under regular conditions.

Condition monitoring of rotational systems is a fast growing area in engineering which focuses on obtaining the criteria for predicting the life cycle, failure type, and fault location in mechanical systems [1]. Sensors and data transmission (wired/wireless) are essential elements in all condition monitoring systems. With the continuous advances in low-power electronics and MEMS, wireless technology allows electronics and sensors to be placed in remote locations.

Wireless communication is a reliable technique for sensory data acquisition which does not have the drawbacks of wired systems such as the need for slip-rings in applications involving rotary motion. The typical wireless sensors use batteries as the power source. Although the size and power storage of batteries has improved over the past years, they still need to be replaced or recharged when used on a continuous basis.

Figure 1.1 shows improvements in the performance of laptop computers on a logarithmic scale over the past few years. Battery energy has the slowest trend of improvement in mobile computing [2].

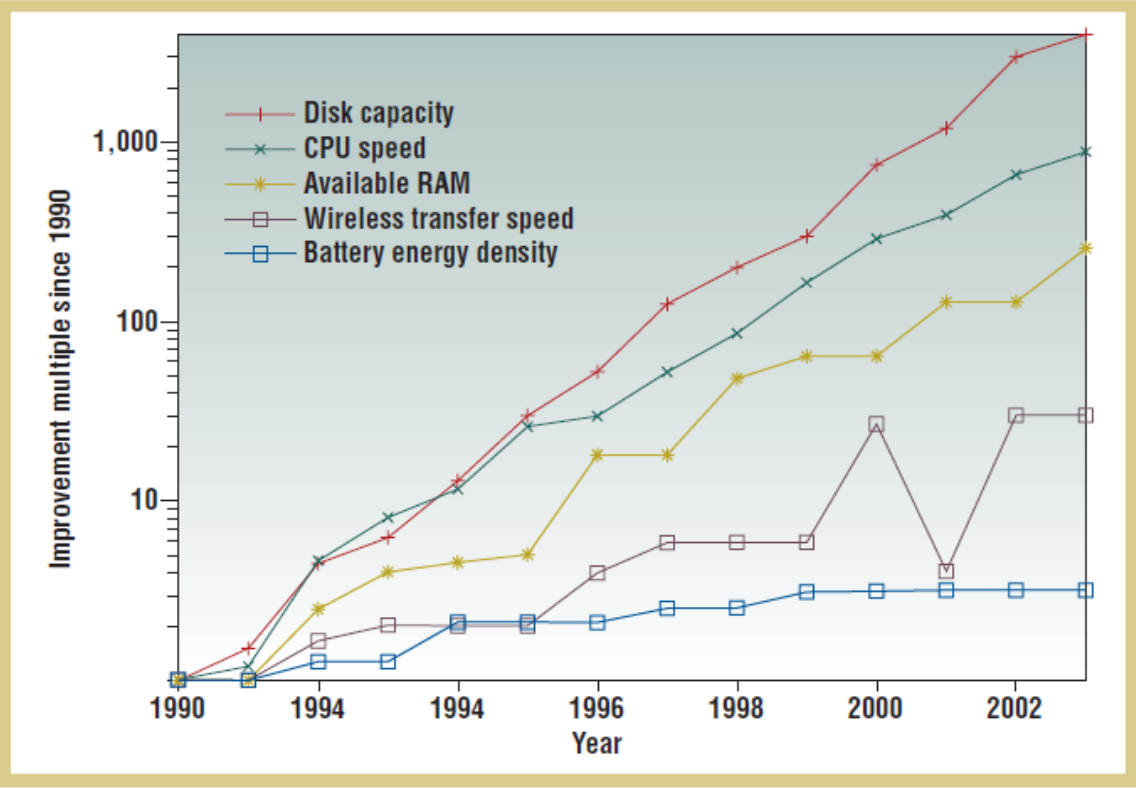

Fig.1.1: Relative improvement in laptop computing technology [2]

Depending on the placement of the sensor on the structure and the location of the structure itself, battery replacement may be challenging or impossible. As a result, availability of an in-situ miniaturized unit that scavenges ambient energy at the location it is installed will be a huge advantage in modern wireless condition monitoring systems.

1.1 Energy Harvesting as a Potential Solution

Harvesting ambient energy is the process of obtaining energy from the environment, converting it into the electricity, and storing it for use by electronic devices. Various sources of ambient energy have been explored in the literature. These sources have advantages such as being essentially free and having clean conversion mechanisms (there is no pollution associated with the conversion process). Energy harvesting technologies include solar, thermoelectric, acoustic, axial-flow micro-turbine and mechanical vibrations. Mechanical vibration as an ambient source of energy for harvesting is described in the next chapter.

Solar energy harvesting is the most common mechanism of power scavenging. Solar panels consist of photovoltaic cells can generate up to 15,000 $\mu W/cm^2$ in direct sunlight [3]. However, their performance reduces to 150 $\mu W/cm^2$ on a cloudy day and only 6 $\mu W/cm^2$ at a desk in an office environment [3].

Thermoelectric energy harvesting devices generate electricity when placed in a temperature gradient. This is the same principle upon which a thermocouple works (the Seebeck effect). Published results indicate that 2.2 $\mu W/cm^2$ can be generated for T = 5 K and 8.6 $\mu W/cm^2$for T = 10 K [4]. Lim and Snyder [5, 6] report a device that generates 40 $\mu W/cm^2$ of power for T = 1.25 K temperature gradient. Strasser *et al*. [7] report a device capable of generating 1 $\mu W/cm^2$ for a T = 5 K.

Acoustic energy harvesters convert energy from acoustic waves into electrical energy. This approach has the major drawback that large areas (about 10 cm^2) and high-level (decibel) sound fields are required to make power scavenging feasible. The power densities for these devices are of the order of 1 $\mu W/cm^2$ at 100 dB [3].

The axial-flow micro-turbine generator can be used when fluid motion is available. Holmes *et al.* [8] developed an axial-flow energy harvester that rotates at 30,000 rpm and generates 1000 μW in a q = 35 ℓ/min airflow, with a differential pressure of Δp = 8 mbar. The device volume is reported to be 0.5 cm^3, which generates power density of 2000 $\mu W/cm^3$. The electrical output (voltage and current) is not reported.

Jansen *et al.* [9] describe how human power can be a viable alternative to batteries in portable consumer products. They examine various forms of human activities and processes such as pushing a button or squeezing a hand to generate enough electrical energy to replace batteries in certain applications. The benefits of such technology to the environment in contrast to batteries are also discussed in this work.

A practical biomechanical energy harvester fabricated by Donelan *et al.* [10] generates electricity during walking with minimal user effort. This device is attached to the knee and harvests energy whenever the knee is extending.

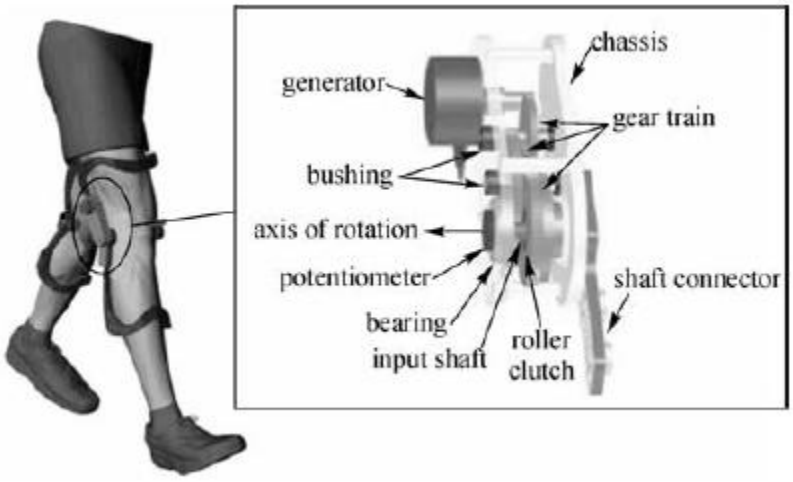

Fig. 1.2: Device configuration of knee-mounted generator by Donelan [10]

1.2 Research objectives

In this research, we found a solution for the problem of charging wireless sensors of health monitoring in rotary motion applications by utilizing a vibration-based energy harvester. A cantilever beam is designed with a tip mass for tuning the natural frequency of the device. Gravity force which is applied to the tip mass is the harmonic excitation to the beam when the hub is rotating. The project objectives include:

- Derivation of the coupled electromechanical model to predict the output of the harvester and analyze the influence of device parameters on its performance.
- Fabricating an experimental setup for testing and verification of the derived model and evaluating performance of the energy harvester.

1.3 Thesis overview

Chapter 2 presents a literature review of different energy harvesting technologies that can be used for extracting energy from vibrations. A review of different techniques and power levels obtained for available energy harvesters is presented. Justification is provided regarding to why the piezoelectric conversion technology was chosen for this research.

In Chapter 3, an introduction to piezoelectricity is provided. Applications of piezoelectric energy harvesters to date are introduced. Fundamental equations of the piezoelectric effect are presented. Existing piezoelectric energy harvesting models are described briefly. Finally a procedure as a guideline to derive a model for a cantilever piezoelectric beam under base excitation is discussed.

Chapter 4 is concerned with the development of the proposed harvester for rotary motion applications by considering the dynamic modeling of a rotating cantilever beam. In this chapter, we show how the equations of motion are derived using the Lagrangian approach and the final coupled electromechanical mode. The closed form solutions for predicting vibration response and the output voltage of the harvester, the optimum resistive load, and the maximum output power of the energy harvester are obtained in this chapter. Effect of different parameters on the harvester dynamics, natural frequency of the device, amplitude of the output power and the optimum resistive load is discussed.

In Chapter 5, simulation results are presented based on the analytical model derived in Chapter 4. Then experimental results on the fabricated prototype are presented. The experimental results are further compared with results from the numerical and analytical studies. The studies indicate close match between analytical developments and experimental results.

CHAPTER 2: VIBRATION-BASED ENERGY HARVESTING

Low-level mechanical vibrations occur frequently in environments such as machinery and vehicles (e.g., an automobile or aircraft). Vibration energy harvesters are designed to convert ambient vibrations into electricity. These devices can be divided into two groups [11]: Non-resonant and resonant energy harvesters (i.e., device resonance frequency is matched to vibration input frequency). A non-resonant energy harvester is more efficient where the input contains very low frequencies (< 10 Hz), and irregular vibrations with amplitudes larger than the device's critical dimensions. Irregular vibrations are defined as inconsistent or discontinuous motions such as the movements of a human body. This configuration finds applications in human movement energy harvesters. On the other hand, the resonant energy harvesters may be utilized in cases where the input vibration source is sustainable with frequencies greater than 100 Hz. In such cases, the vibration source is continuous with stable and well defined spectra, e.g., vibrations generated by an unbalanced machine [11].

To convert the energy from ambient vibrations into electricity, various power harvesting techniques have been developed such as electrostatic, electromagnetic, and piezoelectric harvesters [12]. The above three mechanisms will be discussed in this chapter before focusing on piezoelectric energy harvesting.

2.1 Electrostatic energy harvesting

An electrostatic or capacitive energy harvester works based on the changing capacitance of vibration-dependent variable capacitors. Vibration separates the plates of a variable capacitor which is initially charged. As a result, mechanical vibration energy is converted into electricity. An overview of the different electrostatic harvesters is given by Meninger *et al.* [13]. A main drawback of this method is that a separate voltage source is required to provide an electric field [3]. In contrast, the capacitor configuration can be integrated into micro-systems; so the electrostatic generator is appropriate for scaling into micro dimensions. Meninger *et al.* [13] designed, fabricated, and tested a low-power controller IC for an electrostatic energy harvester. With the proposed control scheme, a usable power output of 5.6 µW was predicted from the generated 8.6 µW total power. Sterken *et al.* [14] introduced the use of an electret (permanently polarized dielectric) for a constant charge supply, thus there was no need for a separate voltage supply anymore. The micro-generator prototype is capable of producing 100 μW electrical power. A major drawback of the electrets is the limited life of the device as the charge degrades over time. Electrostatic generators can be classified into three types [15]:

1. In-plane overlap varying,
2. In-plane gap closing,
3. Out-of-plane gap closing.

These three classes are shown in figure 2.1.

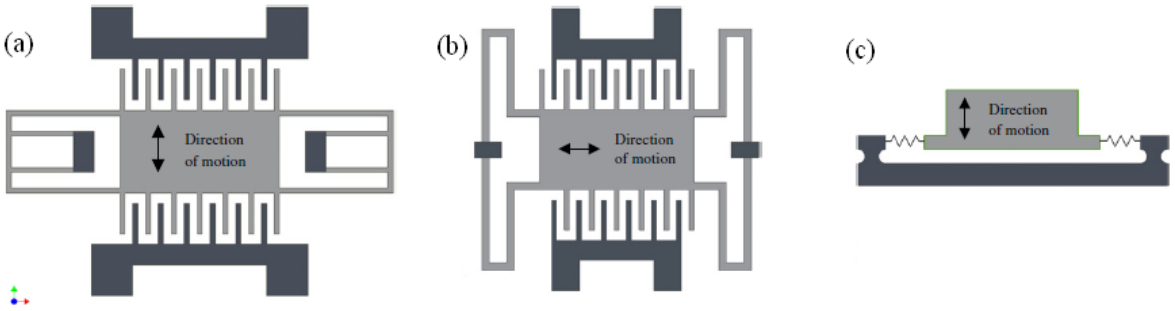

Fig.2.1: Different classes of Electrostatic generators, (a) In-plane overlap varying, (b) In-plane gap closing and (c) out-of-plane gap closing. [15]

2.2 Electromagnetic energy harvesting

The magnetic induction transducer is based on Faraday's law. When a coil is moved within a magnetic field, current flows in the conductor. Vibrations can be converted into electricity by utilizing this mechanism with no need for having a separate voltage source. A main drawback of the magnetic induction transducer is that the permanent magnet needed for creating a permanent magnetic field is bulky. Therefore, it is not conveniently scalable to a MEMS device [3]. Another negative point is that the output voltage from the electromagnetic harvester is normally around 0.1-0.2 V. Therefore, it is necessary to transform the voltage to usable levels. Williams *et al.* [12] fabricated and analyzed an electromagnetic generator for powering remote Microsystems. The fabricated device consists of a permanent magnet that moves relative to a coil. In their work, they derived the equations of motion for a generator consisting of a seismic mass on a spring and a damper.

The power output was derived from the energy that could be dissipated through the damper by converting mechanical to electrical energy. Based on the derived equations, the power output of such a generator is proportional to the cube of the vibration frequency and that the deflection of the seismic mass should be as large as possible. The proposed harvesting system utilized an electromagnetic harvesting scheme. For a generator of the size 5 mm x 5 mm x 1 mm, they predicted 1 μW at an excitation frequency of 70 Hz and 0.1 mW at 330 Hz [12].

El-hami *et al.* [16] described design parameters for the electromagnetic harvester. They developed a generator that extracts more than 1mW within a volume of 240 mm^3. Their device is depicted in figure 2.2.

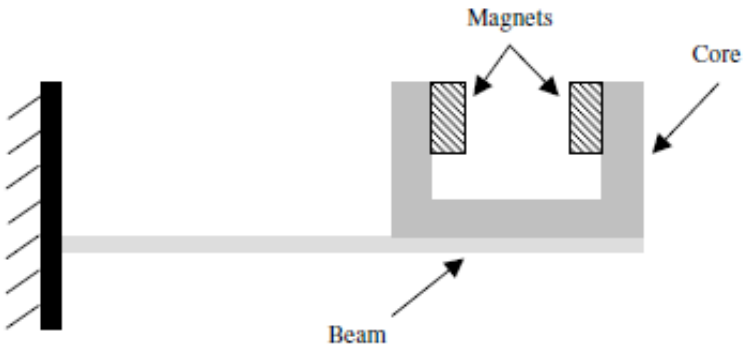

Fig.2.2: The electromagnetic generator designed by El-hami [16]

2.3 Piezoelectric energy harvesting

Piezoelectric elements are physically deformed in the presence of an electric field and inversely produce electrical charge when they are mechanically deformed. The energy density of piezoelectric transducers is three times higher when compared to

electrostatic and electromagnetic transducers [3]. Due to this fact, there is a growing interest in the application of piezoelectric energy harvesters for converting mechanical vibrations into electricity. An overview of research on piezoelectric energy harvesters was discussed by Anton and Sodano [17]. Some of the different types of the piezoelectric materials are ceramics, single crystals, polymers and thin films. Once a piezoelectric material is selected, a mechanical energy harvester can be fabricated using laser micromachining or piezoelectric fibers. Figure 2.3 shows a micro-machined bimorph cantilever piezoelectric energy harvester fabricated by *MIDE* Inc.

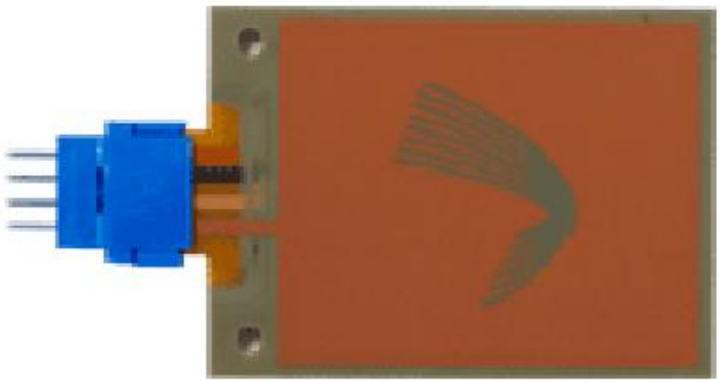

Fig.2.3: Bimorph cantilever piezoelectric energy harvester

Piezoelectric elements in different geometries are available. The most common type is the cantilever beam which is also the focus of this work. Table 2.1 shows a summary of the comparison of the three conversion mechanisms.

Table 2.1: Summary of the comparison of three mechanisms for energy harvesting

Mechanism	Advantages	Disadvantages
Piezoelectric	No voltage source needed Output voltage is sufficient	More difficult to integrate in micro-systems
Electrostatic	Easier to integrate in micro-systems	Separate voltage source needed Has practical difficulties
Electromagnetic	No voltage source needed	Output voltage is low

2.4 Hybrid energy harvesters

A hybrid energy harvester contains different energy harvesting mechanisms. For example, Yang *et al.* [18] investigated a novel energy harvester integrated with piezoelectric and electromagnetic mechanisms. It contains a piezoelectric cantilever, permanent magnets and substrate of two-layer coils. The power density from this device is 790 $\mu W/cm^3$ from piezoelectric components and 0.85 $\mu W/cm^3$ from electromagnetic elements.

Also, There exist other energy harvesters which can convert ambient energy from a source different from vibration into electricity besides vibration energy harvesting. For example, certain products manufactured by *MIDE* named “vulture solar energy harvesters (SEH20W and SEH25W)” convert vibrations and solar energy into useable

electrical energy. This device is a stack of 2 piezos that a solar cell is attached on its sides.

As it was noted in this brief introduction to piezoelectric energy harvesters, the main advantages of using piezoelectric materials compared to electrostatic and electromagnetic transduction mechanisms are large power densities and ease of application. As a result, piezoelectric energy harvesting has received growing attention. In the next chapter, this efficient transduction mechanism is described in detail.

CHAPTER 3: PIEZOELECTRIC ENERGY HARVESTING

In the previous chapter, piezoelectric energy harvesting was introduced as an efficient technique for harvesting ambient vibrations. In this chapter, the piezoelectricity phenomena will be reviewed and various energy harvester designs in the literature that are fabricated based on this property will be introduced. The literature review will also include mathematical modeling of piezoelectric harvesters and discussions regarding the power generation estimations.

3.1 The Piezoelectricity effect and its history

In 1880, Jacques and Pierre Curie discovered: when some specific crystalline materials are subjected to mechanical stress, their crystals become electrically polarized [19]. The polarity is proportional to the applied force. Also, when the crystalline material is subjected to the electric field, mechanical deformations happen due to the polarity of the electric field [20, 21]. The piezoelectricity effect in crystals happens as a result of asymmetry in the cell unit and the generation of electric dipoles due to the mechanical deformation causing a polarisation at the crystal surface, i.e. figure 3.1. Direction of polarization could be reversed if an electric field applied. In this case, a hysteresis field is formed and the material is called ferroelectric.

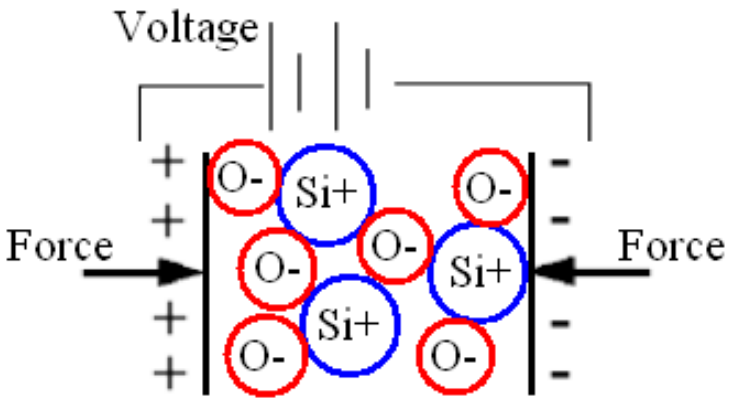

Fig.3.1: Piezoelectric effect molecular overview [22]

A single crystal of ferroelectric material has multiple regions with uniform polarisation named ferroelectric domains when it is grown [23]. In each ferroelectric domain, all the electric dipoles are aligned in the same direction. These domains are separated by boundaries called domain walls. Figure 3.2 illustrates this poling process.

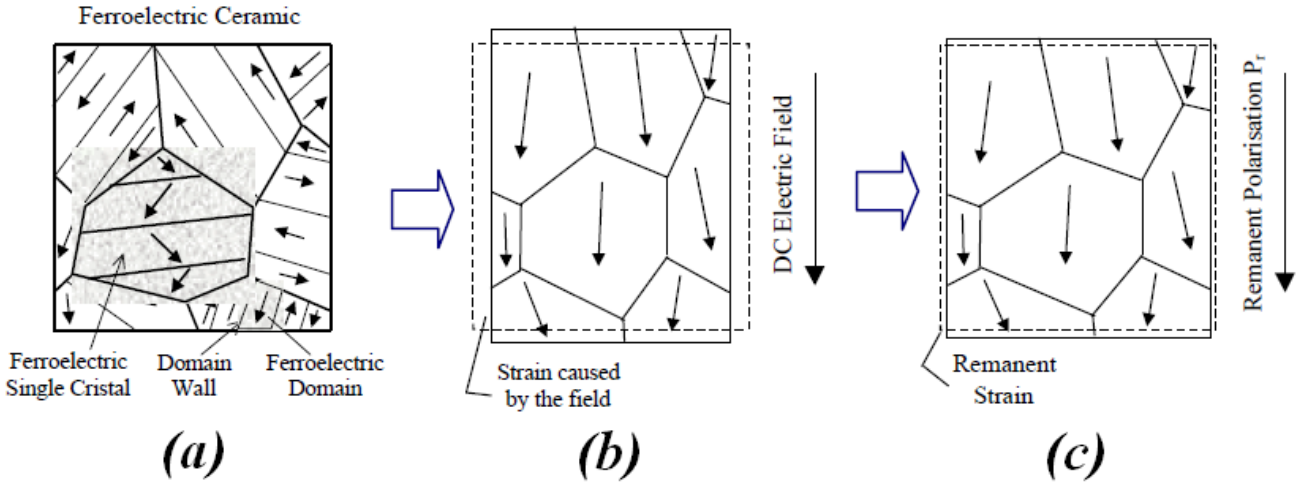

Fig.3.2: Schematic of the poling process in ferroelectric materials [23]

Although Curie's discovery was novel, the first practical applications came a few decades later. In 1918, Langevin developed an ultrasonic submarine detection technique using a quartz-based piezoelectric transducer [25]. This device, also known as sonar, was subsequently used during both world wars. It is also generally accepted that the use of quartz for stabilization of oscillators in the 1920s initiated the field of frequency control. Further developments in piezoelectricity took place in the 1950s and 1960s when studies focused on polymers and their properties [25]. In 1954, PZT (Lead Zirconate Titanate) the most widely used piezoceramic was discovered by Jaffe *et al*.[21]. In 1969, Kawai discovered strong piezoelectric properties in polyvinylidene fluoride [26]. This breakthrough resulted in huge interest in research and applications of this material. Recently, there are numerous applications for piezoelectric materials such as force sensors, accelerometers, filters, resonators, high voltage devices, ultrasonic transducers, and medical ultrasound.

Piezoelectric materials can be put into three categories: Ceramics, Crystalline structures, and Polymers. PZT is an example of piezoceramic, Quartz and Rochelle salt are crystalline piezoelectrics and PVDF is a polymer.

3.2 Piezoelectric energy harvesters

Hausler and Stein (1984) presented one of the earliest experiments on piezoelectric materials energy harvesting application. Their experiment involved a PVDF film inserted into the rib cage of a mongrel dog. This energy harvester was developed for medical applications, and it was predicted that it could generate power on the order

of 1 mW. However, a mechanical simulation of the dog's ribs provided only 20 μW, and the actual experiment only provided 17 μW at a peak voltage of 18 V [27].

Schmidt (1992) investigated the feasibility of using PVDF film in compression to harvest energy from a windmill. The large high-speed rotor used for conventional generators poses a serious safety problem to people nearby. He predicted an output on the order of 100 watts per cubic centimeter, but the material costs still outweigh the perceived benefits and his proposed device has yet to be constructed [28].

Starner (1996) studied the idea of harvesting energy from a living creature, specifically a human being. He performed some theoretical calculations on the amount of power that might be generated from harvesting body heat, respiration, or blood pressure. His conclusion was that harvesting energy from human walking would be the most practical and least intrusive method [29]. The application of piezoelectric materials at the joints of the human body and the piezoelectric shoe inserts have been described in that paper.

Umeda *et al.* (1996) used a piezoelectric transducer to transform mechanical impact energy of a falling steel ball into electric energy [30]. The following year, Umeda *et al.* (1997) presented the results of a prototype generator based on the concept of their earlier work where the effects of the size of the storage capacitor were examined [31].

Kymissis *et al.* (1998) investigated the concept of using PVDF and piezoceramics to harvest energy inside of a shoe. The PZT and PVDF integrated smoothly with a running sneaker, but the magnetic generator was too bulky and obtrusive for practical

use. They measured roughly 1 mJ per step for a PVDF and 2 mJ per step for a PZT unimorph device [32].

In 1998, Kimura patented a piezoelectric generation device that accumulated electric charge after rectifying the AC voltage generated. The source of the generated power was a free-vibrating piezoelectric plate [33].

Goldfarb and Jones (1999) investigated the efficiency of generating power with piezoceramics, specifically by a PZT stack. The stack had poor efficiency because most of the power generated was absorbed back into other layers of the structure [34].

Allen and Smits (2000) presented harvesting energy using the Karman vortex behind a bluff body from induced oscillations of a piezoelectric membrane. Four different membranes were tested, and their behavior was successfully predicted by the proposed models [35].

Ramsay and Clark (2001) studied the feasibility of using piezoelectric material as a power supply for an *in vivo* MEMS application. A square PZT-5A thin plate was driven by a fluctuating pressure source designed to simulate blood pressure. They concluded that with an effective surface area of 1 cm^2 a piezoelectric generator may be able to run a device that require power in the order of μW continuously and a device with mW power requirement intermittently [36].

Elvin *et al.* (2001) worked on the idea of using a strain sensor for energy harvesting and sensing simultaneously. For verification, a PVDF film was attached to a beam for a four-point bending test. The power generated was enough to generate wireless signals in a laboratory setting. The response of the sensor turned out to be

dependent on both the frequency and the applied load, though the sensor successfully measured as low as 60 με [37].

Ottman *et al.* (2002) presented a method of optimizing the harvested energy from a vibrating piezoelectric device using a step-down DC-DC converter. The maximum amount of energy harvested was claimed to be 30.66 mW [38].

Sodano *et al.* (2003) investigated the possibility of using piezoelectric generators to recharge nickel metal hydride batteries. Two types of harvesters, a monolithic piezoelectric (PZT) and a Macro Fiber Composite (MFC), were used for the experiment. The study shows the use of electrodes in the MFC limits the amount of current produced. It was also shown that charging a battery by vibrating the PZT at resonance typically took less time than by using a random input signal to the PZT [39].

Granstrom *et al.* (2007) developed an energy harvesting system for generating electricity from a backpack instrumented with piezoelectric shoulder straps [41]. As the PVDF shoulder straps have almost identical mechanical properties in comparison with nylon straps commonly used; the energy is extracted from an ambient source that is previously lost.

Khameneifar and Arzanpour (2008) looked at the feasibility of piezoelectric energy harvesting from pneumatic tires. The authors predicted 8.4 mW electrical power output from the system [42]. Figure 3.5 shows this concept.

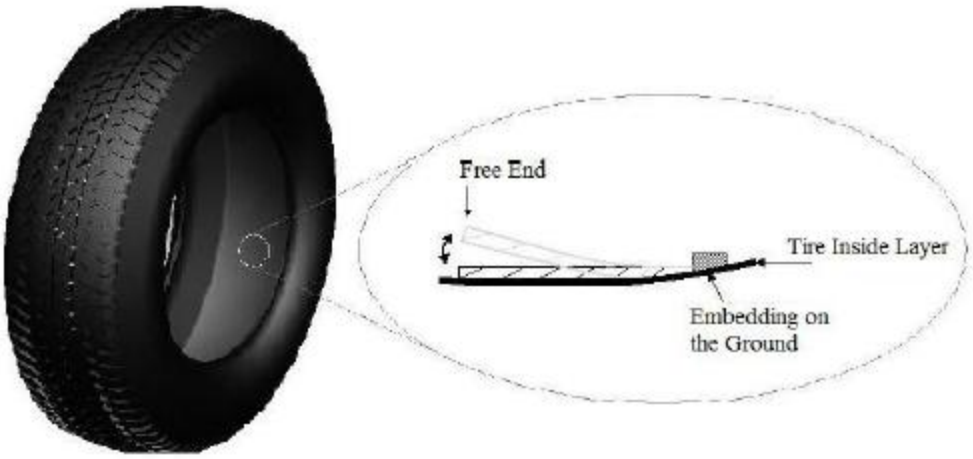

Fig. 3.3: Schematic of the piezoelectric energy harvesting from pneumatic tires

Erturk *et al.* (2009) developed a cantilever piezoelectric energy harvester from an L-shaped beam-mass structure with an application to the landing gears in unmanned air vehicle [43]. Khameneifar, Arzanpour and Moallem (2010) also investigated the possibility of harvesting energy from a PZT decoupler retrofitted in a hydraulic engine mount [44].

3.3 Piezoelectric Energy Harvesting Models

Coupled electromechanical models of piezoelectric materials are derived for design and performance analysis of energy harvesters. Using the 1-D configuration shown in figure 3.6 the constitutive relations can be simplified as, [46]

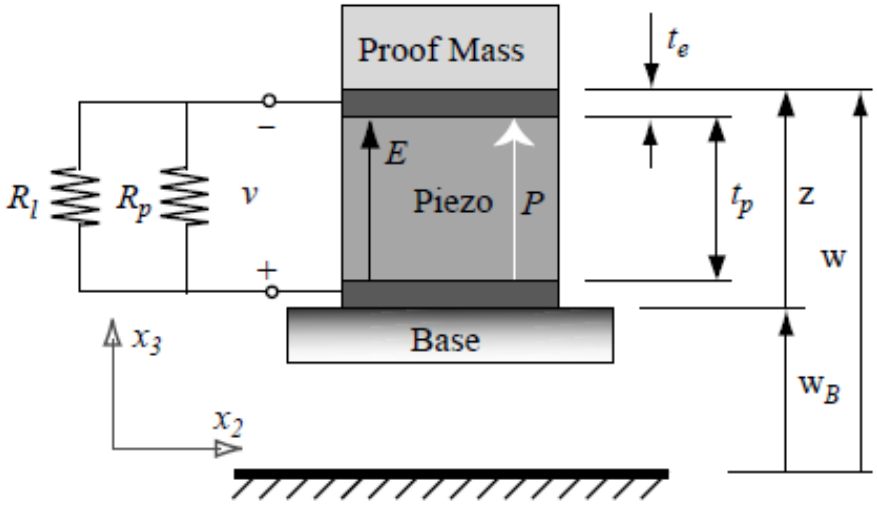

Fig.3.4: 1D model of a piezoelectric energy harvester [46]

$$\begin{Bmatrix} T \\ D \end{Bmatrix} = \begin{bmatrix} C^E & -e^t \\ e & \varepsilon^s \end{bmatrix} \begin{Bmatrix} S \\ E \end{Bmatrix} \tag{3.1}$$

$$T_3 = c_{33}^E S_3 - e_{33} E_3 \tag{3.2}$$

$$D_3 = e_{33} S_3 + \varepsilon_{33}^S E_3 \tag{3.3}$$

The D, E, S, and T matrices are determined as electric displacement, electric field, strain and stress respectively. $\boldsymbol{\varepsilon}$ is the permittivity of the piezoelectric element and e is the piezoelectric constant. The piezoelectric constitutive relations can be used to obtain lumped parameter model of the coupled electromechanical system. Development of the lumped model (SDOF model) was followed by Roundy *et al.* [3] and duToit *et al.*

[46]. They used the 1D configuration to find the governing equation of the energy harvesting system shown in figure 3.5. The governing equations [46] are derived as,

$$\ddot{w} + 2\zeta_m \omega_N \dot{w} + \omega_N^2 w - \omega_N^2 d_{33} v = -\ddot{w}_B \tag{3.4}$$

$$R_{eq} C_p \dot{v} + v + m_{eff} R_{eq} d_{33} \omega_N^2 \dot{w} = 0 \tag{3.5}$$

where ζ_m is mechanical damping ratio, ω_N is natural frequency of the harvester and $m_{eff} = M + \frac{1}{3} m_p$ is the effective mass. d is the piezo constant relating charge density per stress and is related to e through $d = (c^E)^{-1} e$, v is the voltage and *w* is the beam deflection . The equivalent resistance, R_{eq}, is the parallel resistance of the load and the piezoelectric leakage resistance. The leakage resistance, R_p, is usually much higher than the load resistance, R_l,; so R_{eq} is almost equal to R_l. Finally, the capacitance, C_p, is defined as $\varepsilon_{33}^S A_p / h$.

Lumped-parameter model lacks dynamic mode shape of the beam, accurate strain distribution as well as their effects on the electrical response. Therefore, it cannot predict dynamic behaviour of the system accurately, however it gives initial insight into the problem. An improved approach is the Rayleigh-Ritz method which is used by Sodano *et al.* [49]. This method gives a discrete model (an approximate representation) of the distributed parameter system and is more accurate compared to SDOF model. Recently, Erturk and Inman proposed a coupled distributed solution for a piezoelectric energy harvester under base excitation [48], which is experimentally validated [50]. It was shown

that the analytical solution could accurately predict the voltage output and the vibration behaviour of the bimorph.

3.4 Fundamental assumptions of the coupled distributed parameter model

The piezoceramic layers of a bimorph cantilever can be studied in voltage or current mode [51]. The expression bimorph means two piezoceramic layers attached to both sides of the cantilever beam where whole the beam covered by piezo. If only one piezoceramic is attached to one side of the cantilever, the energy harvester is a unimorph. Figure 3.5 shows two bimorph cantilever configurations.

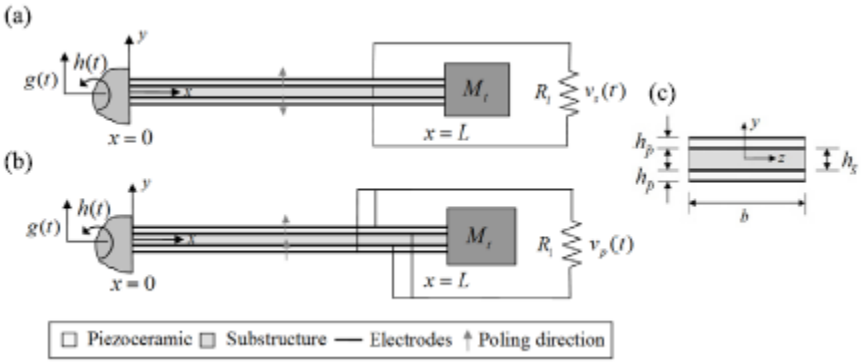

Fig.3.5: (a) series connection of piezoceramic layers, (b) parallel connection of piezoceramic layers and (c) cross sectional view of a bimorph cantilever [50]

The cantilever beam is modeled based on the Euler-Bernoulli beam assumptions. Mechanical damping is represented by internal and external damping mechanisms. The internal damping is assumed to be in the form of strain rate damping and the air resistance is the source of external damping [50].

When the piezoelectric plates are bonded to a cantilever beam; one should find the stress distribution along the beam as a function of excitation frequency. Here a simple step-by-step procedure is described as a guideline to find the stress distribution along the beam:

1. Using the governing equation of motion, find the relative displacement as a function of position and time. The curvature and transverse displacement of the beam can be defined from the Euler-Bernoulli beam equation, Eq. (3.6) where $\boldsymbol{\zeta} = x/L$ is the normalized position *x* along the beam with the length of the beam given by *L*, *E* is the Young's modulus, *I* is the area moment of inertia, ρ is the mass density, and *A* is the cross sectional area of the beam.

$$EI\frac{\partial^4 w(\zeta,t)}{\partial \zeta^4} + \rho A L^4 \frac{\partial^2 w(\zeta,t)}{\partial t^2} = 0 \tag{3.6}$$

2. The boundary conditions are applied to solve the differential equation. For the cantilever beam of mass *m* and tip mass M_L, the boundary conditions are given as Eqs. (3.7):

$$w(0,t) = \frac{\partial w}{\partial \zeta}(0,t) = 0,$$

$$\frac{\partial^2 w}{\partial \zeta^2}(1,t) = 0, \tag{3.7}$$

$$El\frac{\partial^3 w}{\partial \zeta^3}(1,t) = M_L \frac{\partial^2 w}{\partial \zeta^2}(1,t)$$

3. Using separation of variables method, the solution for governing equation is obtained. The general solution for the Euler-Bernoulli equation is,

$$w_i(\zeta, t) = \varphi(\zeta).\delta(t)$$

$$\varphi(\zeta) = C_1 \cos\lambda\zeta + C_2 \sin\lambda\zeta + C_3 \cos h\lambda\zeta + C_4 \sin h\lambda\zeta \tag{3.8}$$

4. Applying boundary conditions, the solution equation is solved for unknown C's. The natural frequency of the beam is then calculated from the Eq. (3.9) which is obtained from the decoupled equation of Euler-Bernoulli beam:

$$\omega_r = \frac{1}{2\pi}\lambda^2\sqrt{\frac{EI}{\rho A}} \tag{3.9}$$

5. The solution for temporal coordinate term $\boldsymbol{\delta(t)}$ is obtained from the equation of motion. The solution of Eq. (3.6) with boundary conditions of Eq. (3.7) for a cantilever beam of mass *m* with a tip mass M_L has been derived by Erturk and Inman [43] as follows:

$$w_i(\zeta, t) = \varphi(\zeta)\delta(t) = \omega^2 \sum_{r=1}^{\infty} \frac{\varphi(\zeta)(\psi)}{\omega_r^2 - \omega^2 + i2\zeta\omega_r\omega} \tag{3.10}$$

Where

$$\varphi(\zeta)=C_r\{\cos\lambda\zeta-\cosh\lambda\zeta-\beta[\sin\lambda\zeta-\sinh\lambda\zeta]\}$$

$$\beta=\frac{m(\sin\lambda-\sinh\lambda)+\lambda M_L(\cos\lambda-\cosh\lambda)}{m(\sin\lambda+\cosh\lambda)-\lambda M_L(\sin\lambda-\sinh\lambda)}$$

$$\delta(t)=\frac{\psi\omega^2}{\omega_r^2-\omega^2+i2\omega\omega_r}y_0e^{j\omega t} \tag{3.11}$$

$$\psi=-m\int_0^1\varphi(\zeta)d\zeta+M_L\varphi(1)$$

6. Taking second partial derivative of transverse displacement $w_i(\zeta,t)$ gives the strain ε on surface of the beam at a distance *y* from the neutral axis as eq. (3.12):

$$\varepsilon(\zeta)=-y\frac{\partial^2 w}{\partial\zeta^2} \tag{3.12}$$

7. Then the Hooke's law can be used to approximately find the stress as a function of distance from the fixed end to the specific location on the beam

$$\sigma(\zeta)=E\varepsilon(\zeta) \tag{3.13}$$

8. Assuming that the material is linear, elastic and isotropic with an average stress applied along the 1-1 direction. It means that the stress is applied in direction perpendicular to direction in which ceramic element is polarized. In this situation

the output voltage from PZT can be obtained by multiplying the stress at the specific location of the piezoelectric element with the piezo voltage constant, ν_{31}:

$$V(\zeta) = \nu_{31} E \varepsilon(\zeta) \tag{3.14}$$

9. Then the output power of the PZT when it is connected to a resistive load, R_L, is given as:

$$P = \frac{V^2}{R_L} = \frac{1}{R_L}\{\nu_{31} E \varepsilon(\zeta)\}^2 \tag{3.15}$$

Erturk and Inman validated this approach in base excitation. The energy harvesting application which is presented in this thesis is based on the tip mass gravitational force fluctuations in a rotational motion. For derivation of the equations of motion an approach similar to Erturk and Inman is followed. Chapter 4 describes the approach of modeling the proposed energy harvester.

CHAPTER 4: DYNAMIC MODELING OF A ROTATING CANTILEVER BEAM WITH PIEZOELECTRIC ELEMENT

In this chapter, we derive a mathematical model of the energy harvester that relates mechanical deflections, hub speed, and other parameters with the generated electric charge. To this end, the coupled dynamic model of a rotating flexible beam are derived and integrated with electrical circuit equations based on the effect of piezoelectric transducer. Equations are solved to extract closed form expressions for vibration response and electrical output of the system. Effect of different parameters on the harvester dynamics analyzed in this chapter. The parameters include beam length, tip mass, damping and piezoelectric material properties such as piezoelectric constant, compliance and relative permittivity.

4.1. Dynamic Modelling of the Rotating Beam

The proposed energy harvester consists of a cantilever beam carrying a tip-mass payload which is mounted on a rotating hub as shown in Fig. 4.1. The cantilever beam contains layers of piezoelectric materials which cover the whole length of the beam. In the system shown in Fig. 4.1, the acceleration of the hub and the gravity force on the tip-mass provide excitations to the system which cause the beam to vibrate.

It should be noted that in the most applications like turbines, the hub rotates with a relatively constant speed during its operation. Thus we assume a constant rotating speed of the hub at the end of dynamic modelling. As a result, gravity will be the only effective driving force for vibrations when the hub is rotating with a constant speed.

As shown in the figure, the hub is rotating about the 'Z' axis, and gravity is acting along the negative 'Y' axis. The main source of vibration input to the harvester is the alternating gravitational force on the cantilever beam.

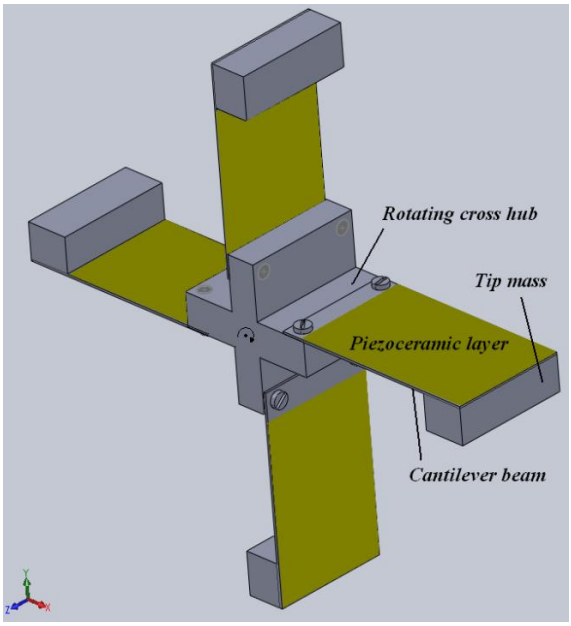

Fig.4.1: Schematic view of the energy harvester for rotary motion applications

The concept is shown in figure 4.2 for one cycle of rotation of one of the four cantilever beams. When the beam is in position (a), the gravitation force on the tip mass applies a bending moment on the cantilever beam in -Z direction. As the beam reaches position (b), the bending moment on the cantilever beam is zero. At position (c) the

bending moment caused by the tip mass is in +Z direction. Position (d) is identical to (b), where the effect of tip-mass gravitational force is zero.

As a result, a full turn of the hub applies an alternating force on the harvester. The frequency of the force alternation is as same as the hub rotation frequency. Thus the induced vibration generates a harmonic voltage on the piezoelectric element that is a function of the strain applied to this element.

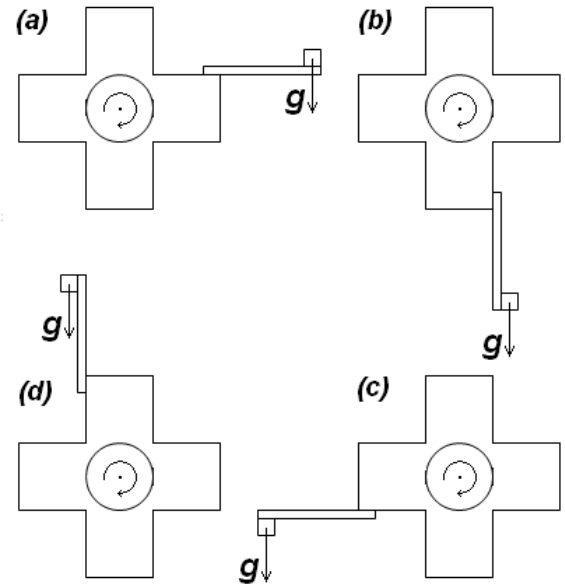

Fig.4.2: Orientation of the beam and gravitational force in one cycle of rotation

Deflection of the beam relative to its base is denoted by $w(\xi, t)$ where $\xi = x/L$ is the normalized position *x* along the beam with the length of the beam given by *L.* Assuming an Euler-Bernoulli beam with small deformations, the partial differential equation describing vibrations of the cantilever beam is given by [48]

$$EI\frac{\partial^4 w(\xi,t)}{\partial \xi^4} + \rho AL^4 \frac{\partial^2 w(\xi,t)}{\partial t^2} = 0 \tag{4.1}$$

where *E* is the Young's modulus, *I* is the area moment of inertia, ρ is the mass density, and *A* is the cross sectional area of the beam. The piezoelectric layers cover the whole length of the beam; hence EI and ρA are taken as constant values. It should be noted that placing the piezo layers on a part of the beam would not be appropriate if the device is to be used as an energy harvester as the goal is to extract maximum power by utilizing the whole length of the beam. Using the method of separation of variables, $w(\xi, t)$ can be decomposed as

$$w(\xi,t) = \varphi(\xi).\delta(t) \tag{4.2}$$

where $\varphi(\xi)$ and $\delta(t)$ are spatial and temporal coordinate systems. Moreover

$$\delta_i(t) = e^{j\omega t}\ ,\ \omega^2 = \frac{\beta^4 EI}{\rho AL^4} \tag{4.3}$$

$$\varphi_i(\xi) = c_1 \sin\beta\xi + c_2 \cos\beta\xi + c_3 \sinh\beta\xi + c_4 \cosh\beta\xi \tag{4.4}$$

where (4.4) describes the *i*-th mode shape of the beam. The boundary conditions of (4.1) specify an infinite set of values for β. Each β determines an eigenfrequency ω of the beam. The terms in (4.4) can be determined by incorporating boundary conditions of

the system. The following boundary conditions can be considered for a clamped-free beam carrying a load tip-mass

$$\varphi_i(\xi)|_{\xi=0} = 0 \ , \qquad \frac{d\varphi_i(\xi)}{d\xi}|_{\xi=0} = 0 \tag{4.5}$$

$$\frac{d^2\varphi_i(\xi)}{d\xi^2}|_{\xi=1} = \frac{J_L\beta^4}{\rho AL^4}\frac{d\varphi_i(\xi)}{d\xi}|_{\xi=1} \tag{4.6}$$

$$\frac{d^3\varphi_i(\xi)}{d\xi^3}|_{\xi=1} = -\frac{M_L\beta^4}{\rho AL^4}\varphi_i(\xi)|_{\xi=1} \tag{4.7}$$

where M_L and J_L are the load mass and inertia, respectively. Using the above boundary conditions we have

$$c_3 = -c_1 \, , c_4 = -c_2 \tag{4.8}$$

It can be shown that the positive value of β is given by the solutions of the following equation

$$\begin{aligned}(1 + \cos\beta\cosh\beta) - M\beta(\sin\beta\cos\beta - \cos\beta\sinh\beta) \\ - J\beta^3(\sin\beta\cosh\beta + \cos\beta\sinh\beta) + MJ\beta^4(1 - \cos\beta\cosh\beta) = 0\end{aligned} \tag{4.9}$$

where $M = \frac{M_L}{\rho A L^4}$ and $J = \frac{J_L}{\rho A L^4}$. By using the method of assumed modes [47], [48], and the Lagrangian formulation, the dynamic model for the beam is obtained by using

$$\frac{d}{dt}\left(\frac{\partial T}{\partial \dot{q}_i}\right) - \frac{\partial T}{\partial q_i} + \frac{\partial U}{\partial q_i} = F_i \tag{4.10}$$

where *T* is total kinetic energy, *U* is strain energy, F_i is the *i*-th generalized force, and q_i is the *i*-th generalized coordinate. Figure 4.3 symbolizes the flexible beam-mass system in rotation. According to this figure, assume that *R* is the position of an infinitesimal segment on the beam in the rotating coordinate system *X*-Y*.*

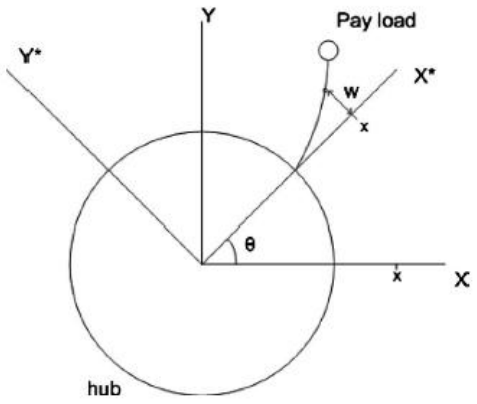

Fig.4.3: Rotating flexible beam-mass system

Then the following relationships can be written

$$R = xi^* + wj^* \tag{4.11}$$

$$\dot{R} = \frac{\partial x}{\partial t} i^* + \frac{\partial w}{\partial t} j^* + \dot{\theta} k^* \times (x i^* + w j^*) = \left(\dot{x} - \dot{\theta} w\right) i^* + (\dot{w} + x\dot{\theta}) j^* \tag{4.12}$$

The kinetic energy of different components of the beam-mass system can be expressed as follows. For the hub:

$$T_{hub} = \frac{1}{2}\left[\int_{hub} (x^2 + y^2) dm\right]\dot{\theta}^2 = \frac{1}{2} J_h \dot{\theta}^2 \tag{4.13}$$

where J_h is hub inertia. For the beam ($\dot{x} = 0, y = 0, \dot{y} = 0$) the kinetic energy is

$$T_{beam} = \frac{1}{2} J_b \dot{\theta}^2 + \frac{1}{2} \int_{beam} \left(\dot{w}^2 + 2\dot{w} x \dot{\theta}\right) dm \tag{4.14}$$

where J_b is the beam inertia. For the tip mass, we have $x = L, \dot{x} = 0, \dot{y} = 0, w(x,t) = w(L,t), \dot{w}(x,t) = \dot{w}(L,t)$. Hence, the expressions for translational and rotational kinetic energies are as follows

$$T_{L_1} = \frac{1}{2}\left[\dot{\theta}^2 w(L,t)^2 + \left(\dot{w}(L,t) + L\dot{\theta}\right)^2\right] M_L \quad \text{(translational)} \tag{4.15}$$

$$T_{L_2} = \frac{1}{2} J_L \left[\dot{\theta} + \frac{\partial \dot{w}(L,t)}{\partial x}\right]^2 \quad \text{(rotational)} \tag{4.16}$$

The potential energy *U* can be expressed as

$$U = \int_0^L \frac{EI}{2} \left(\frac{\partial^2 w}{\partial x^2}\right)^2 dx + g\rho A \int_0^L \left(\frac{w}{\cos\theta} + (x - w\tan\theta)\sin\theta\right) dx + M_L g h|_{\xi=1} \tag{4.17}$$

where $h|_{\xi=1}$ is the deflection of the beam at its end point given by

$$h|_{\xi=1} = \left(\frac{w|_{\xi=1}}{\cos\theta} + (L - w|_{\xi=1}\tan\theta)\sin\theta\right) \tag{4.18}$$

Let us consider the generalized coordinates as

$$q_1 = \theta, q_2 = \delta_1, \ldots, q_{m+1} = \delta_m \tag{4.19}$$

Then the generalized applied forces are given by $F_1 = T,$ which is the torque applied on the rotating shaft, and F_P which is the moment induced by the piezoceramic layer [51] are given as follows

$$F_1 = T, F_2 \; to \; F_{m+1} = F_P = \kappa v(t)\begin{bmatrix} \varphi_1'(a) - \varphi_1'(b) \\ \vdots \\ \varphi_m'(a) - \varphi_m'(b) \end{bmatrix} \tag{4.20}$$

In equation (4.20), it is assumed that a pair of piezoceramics are mounted with their two ends located at x_a and x_b of the beam. In this paper we have $x_a = 0$, $x_b = L$. It should be noted that this torque is a function of voltage $v(t)$ applied to the piezoceramic layer. The term κ is a backward coupling term given by [52]

$$\kappa = \frac{h_1 t_z (t_z + 2h_1) E_z}{{h_1}^3 + (t_z^3 + 3h_1 t_z^2 + 3{h_1}^2 t_z)\,{E_z}/{E}}\, w_1 {h_1}^2 \frac{d_{31}}{t_z} \tag{4.21}$$

where d_{31} is the charge constant; E, E_z are the modulus of elasticity of the beam and PZT, respectively; $2h_1$ is the thickness of the beam; w_1 is the width of the beam; and t_z is the thickness of the piezoelectric layer. Applying the Lagrangian formulation for all generalized coordinates would result in m+1 equations which can be presented in matrix form as follows

$$M(\delta)\begin{bmatrix}\ddot{\theta}\\ \ddot{\delta}\end{bmatrix} + C\left(\delta, \theta, \dot{\delta}, \dot{\theta}\right)\begin{bmatrix}\dot{\theta}\\ \dot{\delta}\end{bmatrix} + G(\delta, \theta) + \begin{bmatrix}0\\ K\delta\end{bmatrix} = \begin{bmatrix}T\\ F_P\end{bmatrix} \tag{4.22}$$

where δ is $[\delta_1, \dots, \delta_m]^T$. The elements of the mass matrix, m_{ij}, are expressed as

$$m_{11} = J_h + J_b + J_L + M_L L^2 + M_L(\varphi_e^T \delta)^2 \tag{4.23}$$

$$m_{ii} = m_b \varphi_{i-1,e}^2 + M_L \varphi_{i-1,e}^2 + J_L {\varphi'}_{i-1,e}^2 \quad i = 2, \dots, m+1 \tag{4.24}$$

$$m_{ij} = M_L L \varphi_{j-1,e} + J_L {\varphi'}_{j-1,e} + \sigma_{j-1} \quad \begin{cases} i = 1, \dots, m+1 \\ j \neq i \end{cases} \tag{4.25}$$

where φ, φ' and σ are $m \times 1$ vectors with σ_i is given by

$$\sigma_i = \rho A L^2 \int_0^1 \varphi_i(\zeta) d\zeta \qquad i = 1, \dots, m \tag{4.26}$$

Matrix $C(\delta, \theta, \dot{\delta}, \dot{\theta})$ represents Coriolis and Centrifugal terms and can be expressed as

$$C(\delta, \theta, \dot{\delta}, \dot{\theta}) = \begin{bmatrix} M_L(\varphi_e^T \delta)(\varphi_e^T \dot{\delta}) & M_L \dot{\theta}(\varphi_e^T \delta)\varphi_e^T \\ -M_L \dot{\theta}(\varphi_e \varphi_e^T)\delta & 0 \end{bmatrix} \tag{4.27}$$

The elements of the gravitational force vector $G(\delta, \theta) = \begin{bmatrix} G_{11} \\ G_{21} \end{bmatrix}$ are expressed as follows

$$G_1 = G_{11} = \left[g\rho A(-\sin\theta) \int_0^L \varphi^T dx + M_L g(-\sin\theta){\varphi_e}^T \right] \delta + g\rho A \frac{L^2}{2} \cos\theta + M_L g L \cos\theta \tag{4.28}$$

$$G_2 = G_{21} = g\cos\theta \left[\rho A \int_0^L \varphi dx + M_L \varphi_e \right] \tag{4.29}$$

Also, the equivalent-spring constant K is expressed as

$$K = \left(EI \int_0^L \varphi'' {\varphi''}^T dx \right) \tag{4.30}$$

Assuming $H = M^{-1}$ and multiplying (4.22) by H and rearranging the terms we have

$$\begin{bmatrix} \ddot{\theta} \\ \ddot{\delta} \end{bmatrix} = H \begin{bmatrix} T - f_{11} - f_{12} - G_1 \\ F_P - K\delta - f_{21} - f_{22} - G_2 \end{bmatrix} \tag{4.31}$$

where $H = \begin{bmatrix} H_{11} & H_{12} \\ H_{21} & H_{22} \end{bmatrix}_{(m+1)\times(m+1)}$

in which $\mathrm{H}_{12}$is an $\mathrm{m}-$dimensional row vector, $\mathrm{H}_{21} =$

$\mathrm{H}_{12}{}^{\mathrm{T}}$ is an $\mathrm{m}-$dimensional column vector, and $\mathrm{H}_{22}$is an $\mathrm{m} \times \mathrm{m}$ matrix.

Other elements of equation (4.31) are given by $f_{11} = c_{11}\dot{\theta}$, $f_{12} = c_{12}\dot{\delta}$, $f_{21} = c_{21}\dot{\theta}$ and $f_{22} = c_{22}\dot{\delta} = 0$. Thus, the following equations are obtained from (4.31)

$$\ddot{\theta} = H_{11}(T - f_{11} - f_{12} - G_1) - H_{12}(K\delta + f_{21} + G_2 - F_P) \tag{4.32}$$

$$\ddot{\delta} = H_{21}(T - f_{11} - f_{12} - G_1) - H_{22}(K\delta + f_{21} + G_2 - F_P) \tag{4.33}$$

From equations (4.32) and (4.33), and assuming that the hub rotates with a constant speed ($\ddot{\theta} = 0$), the dynamic model of the rotating flexible beam is given by

$$\ddot{\delta} + \left(H_{22} - H_{21}{H_{11}}^{-1}H_{12}\right)\left(K - M_L\dot{\theta}^2\varphi_e\varphi_e^T\right)\delta = -\left(H_{22} - H_{21}{H_{11}}^{-1}H_{12}\right)(G_2 - F_P) \tag{4.34}$$

4.2. Coupled electrical model

Next we obtain the equations describing dynamics of piezoelectric transducer. The piezoceramic layers of a symmetric bimorph cantilever beam can be connected in series or in parallel depending on the application [50]. Figure 4.4 shows that each piezoceramic layer in parallel connection can be represented as a current source in parallel with its internal capacitance. In a practical situation, the output voltage is

rectified and conditioned by the converter circuit for storing the harvested power in a storage media such as a large capacitor. However, the purely resistive electrical load gives a simple and useful way of calculating the power generated from the scavenger which has already been used in different studies [53].

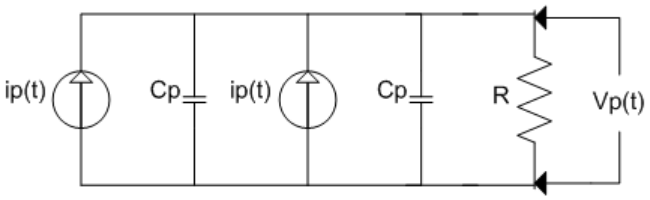

Fig.4.4: Electrical circuit symbolizing the parallel connection of bimorph piezoelectric layers

The electrical circuit equation for the circuit shown in Figure 4.4 can be derived based on the Kirchhoff laws as follows

$$C_p \frac{dv(t)}{dt} + \frac{v(t)}{2R_l} = i_p(t) \tag{4.35}$$

The output current of the PZT sensor is function of strain and given by [52]

$$i_p(t) = -\frac{d_{31} E_z w_1 t_h}{2} \int_0^L \frac{\partial^3 w(x,t)}{\partial x^2 \partial t} dx = -\frac{d_{31} E_z w_1 t_h}{2} \sum_{r=1}^{m} \varphi'^T_{i,e} \dot{\delta}_i \tag{4.36}$$

Where R_l is the load resistance; $C_p = \frac{\varepsilon_{33}^S bL}{h_p}$ is the internal capacitance of each layer; $\gamma = -\frac{d_{31} E_z w_1 t_h}{2} \varphi'_{1,e}$ is the forward coupling term; ε_{33}^S is the permittivity constant; b,

L and h_p are the width, length, and thickness of the piezoceramic layer; and t_h is the thickness of the beam.

4.3. Undamped Coupled Electromechanical Model

The model given by (4.34) is reduced to a single-mode model to simplify the analysis and gain more insight about the dynamic behavior of the system. Thus the single mode model is given by

$$\ddot{\delta}(t) + \frac{(K - M_L\dot{\theta}^2\varphi_{1,e}^2)}{(M_L\varphi_{1,e}^2 + J_L\varphi'^2_{1,e} + m_b\varphi_{1,e}^2)}\delta(t) + \frac{1}{(M_L\varphi_{1,e}^2 + J_L\varphi'^2_{1,e} + m_b\varphi_{1,e}^2)}\kappa\varphi'_{1,e}v(t) = \tag{4.37}$$

$$-\frac{1}{(M_L\varphi_{1,e}^2 + J_L\varphi'^2_{1,e} + m_b\varphi_{1,e}^2)}G_2(t)$$

$$C_p\dot{v}(t) + \frac{v(t)}{2R_l} = -\frac{d_{31}E_z w t_h}{2}\varphi'_{1,e}\dot{\delta}(t) \tag{4.38}$$

An interesting observation from (4.37) is that the stiffness term varies as the hub speed changes. Thus the beam is more *rigid* with a stiffness of *K* when it is not rotating which is reduced by $M_L\dot{\theta}^2\varphi_{1,e}^2$ due to rotational speed. In other words the rotation makes the beam *less rigid* by a factor proportional to the square of the rotational speed. From (4.37), it follows that if we select $\dot{\theta}$ such that $K - M_L\dot{\theta}^2\varphi_e\varphi_e^T > 0$ the dynamic equation is stable since all of coefficients of the equation are positive. If the base moves

fast enough such that $K - M_L\dot{\theta}^2\varphi_e\varphi_e^T < 0$, the dynamic equation (4.37) becomes unstable.

The parameters that affect eigenfrequency of the beam-mass system can be used to design an efficient energy harvester. Proof mass M_L and Beam length *L* influence the eigenfrequency of the system. For a constant angular speed, the resonant frequency of the energy harvester is in the form of $(\tilde{k}_1 + \tilde{k}_2\dot{\theta}^2)^{1/2}$. As M_L increases, both $\tilde{k}_1$ and $\tilde{k}_2$ decrease monotonically. This fact can be used as a design guideline. Hence, by increasing the mass of the proof mass, the resonant frequency of the beam-mass system decreases. Coefficient $\tilde{k}_2$ does not depend on the beam length; however by increasing *L,* the term $\tilde{k}_1$ decreases sharply and as a result the resonant frequency is decreased as the beam length increases.

Equation (4.37) also shows the effect of gravity as the harmonic driving force. The effect of the piezoelectric output (harvested voltage) on the coupled equation of motion can also be observed from (4.38). The electromechanical model that has been derived so far is without considering the effect of damping in the system which is considered in the next section.

4.4. Dynamic Equations Including the Damping Term

The effect of damping can be added to the Euler-Bernoulli equation by incorporating internal strain rate damping and viscous air damping. Hence, let us introduce a damping term with a coefficient $2\zeta_r\omega_r = \frac{c_s\omega_r^2}{E} + \frac{c_a}{m}$ where the first term represents the effect of the strain-rate damping component and the second part

represents air damping component with damping coefficients C_s and C_a, respectively [50]. After substituting the forcing function from equation (4.29) into (4.37) and introducing the above damping term we have

$$\ddot{\delta} + 2\zeta_r \omega_r \dot{\delta} + \omega_r^2 \delta + \frac{X}{B} v = -\frac{A}{B} \cos \dot{\theta} t \tag{4.39}$$

$$C_p \dot{v} + \frac{v}{2R} = \gamma \dot{\delta} \tag{4.40}$$

where $\omega_r = \sqrt{\frac{C}{B}}$, $\gamma = -\frac{d_{31} E_z w t_h}{2} \varphi'_{1,e}$, $A = \left[\rho A \int_0^L \varphi dx + M_L \varphi_e\right] g$, $B = (M_L \varphi_{1,e}^2 + J_L \varphi'^2_{1,e} + m_b \varphi_{1,e}^2)$, $C = \left(K - M_L \dot{\theta}^2 \varphi_{1,e}^2\right)$, $X = \kappa \varphi'_{1,e}$.

Solving equations (4.39) and (4.40) for δ and output voltage *V* in the phasor domain we have

$$V(\dot{\Theta}) = \frac{2j\dot{\Theta} R \gamma A}{D_1 + jD_2} \tag{4.41}$$

$$\delta(\dot{\Theta}) = \frac{A + j2\dot{\Theta} R C_p A}{D_1 + jD_2} \tag{4.42}$$

Where j is the imaginary number and D_1, D_2 are given by

$$D_1 = \left(B + 2RC_p B(2\zeta\sqrt{\frac{C}{B}}) + M_L \varphi_{1,e}^2\right)\dot{\Theta}^2 - K$$

$$D_2 = 2RC_p\left(B + M_L\varphi_{1,e}^2\right)\dot{\Theta}^3 - \left(2R\left(\gamma X + C_p K\right) + 2B\zeta\sqrt{\frac{C}{B}}\right)\dot{\Theta}$$

Using (4.41), the average harvested electrical power is given by

$$|P| = \frac{|V|^2}{R} = \frac{4\dot{\Theta}^2 R\gamma^2 A^2}{[(D_1)^2 + (D_2)^2]} \tag{4.43}$$

Equation (4.43) can be used to derive an expression for the upper bound of the maximum power in terms of load resistance R. The resulting R is the optimum load resistance to be placed across harvester. For this value of resistive load, the power is the maximized which represents an upper bound of the power that can be harvested. To this end, let us rewrite (4.43) as

$$|P| = \frac{\lambda R}{[(\alpha_1 R + \alpha_2)^2 + (\beta_1 R + \beta_2)^2]} \tag{4.44}$$

Where $\lambda = 4\dot{\Theta}^2 R\gamma^2 A^2$, $\alpha_1 = 2C_p\left(B + M_L\varphi_{1,e}^2\right)\dot{\Theta}^3 - 2\left(\gamma X + C_p K\right)\dot{\Theta}$, $\alpha_2 = -2B\zeta\sqrt{\frac{C}{B}}\dot{\Theta}$,

$\beta_1 = 4C_p B\zeta\sqrt{\frac{C}{B}}\dot{\Theta}^2$ and $\beta_2 = \left(B + M_L\varphi_{1,e}^2\right)\dot{\Theta}^2 - K$.

Solving for $\frac{dP}{dR} = 0$, $R_{Optimum}$ is given by

$$R_{Optimum} = \sqrt{\frac{\alpha_2^2 + \beta_2^2}{\alpha_1^2 + \beta_1^2}} \tag{4.45}$$

Substituting $R_{Optimum}$ in the power expression (4.44) results in

$$P_{max} = \frac{\lambda}{2\sqrt{(\alpha_1^2 + \beta_1^2)(\alpha_2^2 + \beta_2^2)}} \tag{4.46}$$

Hence the output power from the harvester cannot be larger than the value of P_{max} at the resonance frequency which is the upper bound of the power that can be harvested from the system. In Eq. (4.45) the effect of damping on the optimal resistive load has been neglected. If one differentiates the expression to obtain the optimal resistance in terms of the damping ratio, the result will show that an increase in damping results in an increase in the value of optimal resistance. In fact, mechanical damping for the mechanical beam-mass system is like the resistance in electrical circuits. For maximizing the power transfer through the harvester one should match the load and source resistances.

4.5. Bimorph Vs. Unimorph configurations

The cantilever used for the energy harvesting application, may contain one or two layers of piezoelectric materials on its length. The first configuration is named Unimorph. In the second configuration, both sides of the beam are covered by the

piezoelectric films which is called bimorph. There are two ways of connecting the electrodes in a bimorph cantilever: Series connection and Parallel connection. If one requires more current in an application, then the series connection will help. The parallel connection results in higher voltages.

To charge the batteries in a wireless sensor system, higher voltages are required. For the parallel connection; the electrical circuit equations are derived as Eq. (4.35) while Eq. (4.47) represents the electric circuit for the unimorph or series connection of a bimorph [50].

$$C_p \frac{dv(t)}{dt} + \frac{v(t)}{R_l} = i_p(t) \tag{4.47}$$

The coupling term, κ, in Eq. (4.20) is defined as Eq. (4.48), (4.49) and (4.50) for unimorph configuration, series and parallel connections, respectively [Energy harvesting technologies [45]]. The subscripts *u*, *bs* and *bp* stand for unimorph, bimorph-series and bimorph-parallel, respectively.

$$\kappa_u = \frac{e_{31} b}{2 h_{pu}} (h_b^2 - h_c^2) \tag{4.48}$$

$$\kappa_{bs} = \frac{e_{31} b}{2 h_{pb}} \left[\frac{h_{sb}^2}{4} - \left(h_{pb} + \frac{h_{sb}}{2} \right)^2 \right] \tag{4.49}$$

$$\kappa_{bp} = \frac{e_{31} b}{h_{pb}} \left[\frac{h_{sb}^2}{4} - \left(h_{pb} + \frac{h_{sb}}{2} \right)^2 \right] \tag{4.50}$$

b is the width of the beam. h_{pu} or h_{pb} is the thickness of the piezoceramic layer. The positions of the bottom and the top of the piezoceramic layer from the neutral axis are denoted by h_b and h_c, respectively. h_{sb} is the thickness of the substructure layer of the bimorph configuration. In this project, experimental study is performed for the energy harvester of unimorph configuration. Also the numerical analysis is based on the unimorph model to be comparable with the experimental results.

4.6. Effect of parameters on the harvester dynamics

In order to design the effective energy harvesters, it is necessary to determine the influence of the harvester parameters on its dynamics. Among the mechanical parameters, the effect of tip mass and dimension of the beam such as its length were described in section 4.3. In this section, the effects of the piezoelectric material constants and mechanical damping on the energy harvesting system is investigated. The variable parameters of a piezoelectric material are piezoelectric constant denoted by d_{31}, elastic compliance constant indicated as s_{11}^E and permittivity constant shown as $\varepsilon_{33}^T / \varepsilon_0$. Effect of these parameters are numerically discussed as simulations are

performed for different values of these parameters while the energy harvesters are geometrically identical and all other parameters of the materials are the same instead of one of these parameters mentioned earlier to see the effect of them on the output power of the energy harvester.

Another parameter whose effect should be considered carefully is the mechanical modal damping of the energy harvester. The brief numerical analysis of this chapter for evaluating the effect of material constants is based on the specifications of *MIDE* PZT that its properties will be described in tables 5.3 and 5.4. Tip mass effect is evaluated by using data from table 5.1 and 5.2. From the spec sheet, the piezo constant of this specific material is $-190\ pm/V$, its compliance constant is $16.5\ pm^2/N$ with the relative permittivity of 1700.

4.6.1. Effect of Piezoelectric constant

In order to investigate the influence of piezoelectric constant d_{31} on the output power of the energy harvesting system, other parameter values including dimensions and material properties should be identical while this constant is changing in the formulas. Figure 4.5 shows the simulation results for this case. The optimum resistive loads are affected, because this load depends on the electromechanical coupling. Referring to figure 4.5, when the piezo constant is higher, the optimal load resistance for the energy harvester tends to be lower while the maximum output power at the natural frequency is not changing. It means that if there is no limit for changing piezo constant value of a piezoelectric material and one changes this parameter from zero to infinity; it results in change of the optimal load while the maximum output power is not changing.

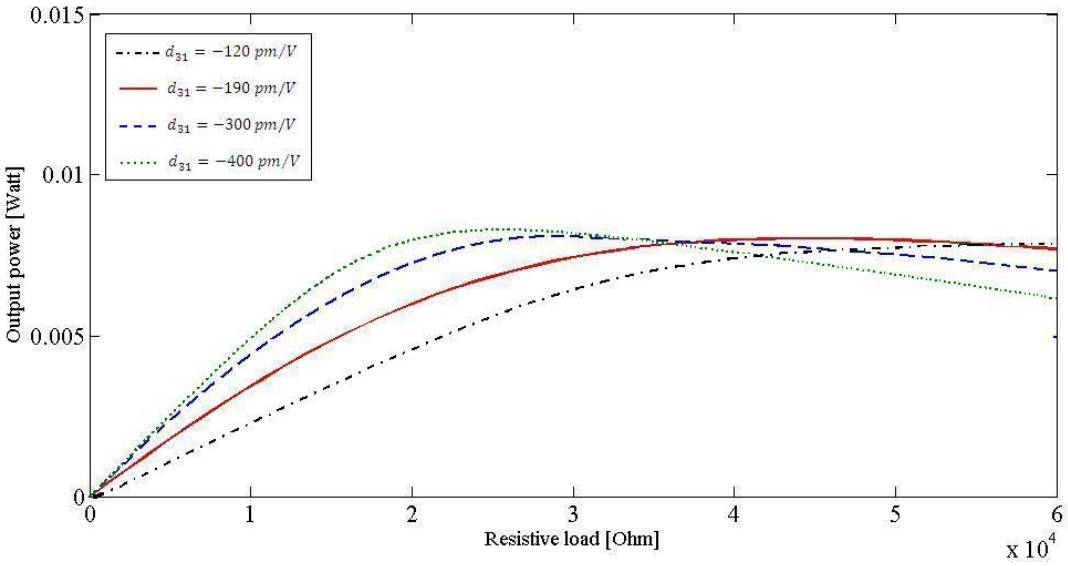

Fig. 4.5: Effect of the piezoelectric constant on the output power and the optimal load resistance

4.6.2. Effect of Compliance

In order to study the effect of elastic compliance of the piezoelectric material on the dynamics of the energy harvesting system, all other parameter values should be consistent while the compliance constant is changed. We consider a range of values for this constant. Figure 4.6 shows that the decrease in the value of this parameter causes the decrease in the value of optimal load resistance and the amplitude of output power. The important thing about this change is that it affects the value of the natural frequency. As the material has higher value of stiffness, so the natural frequency has the higher value.

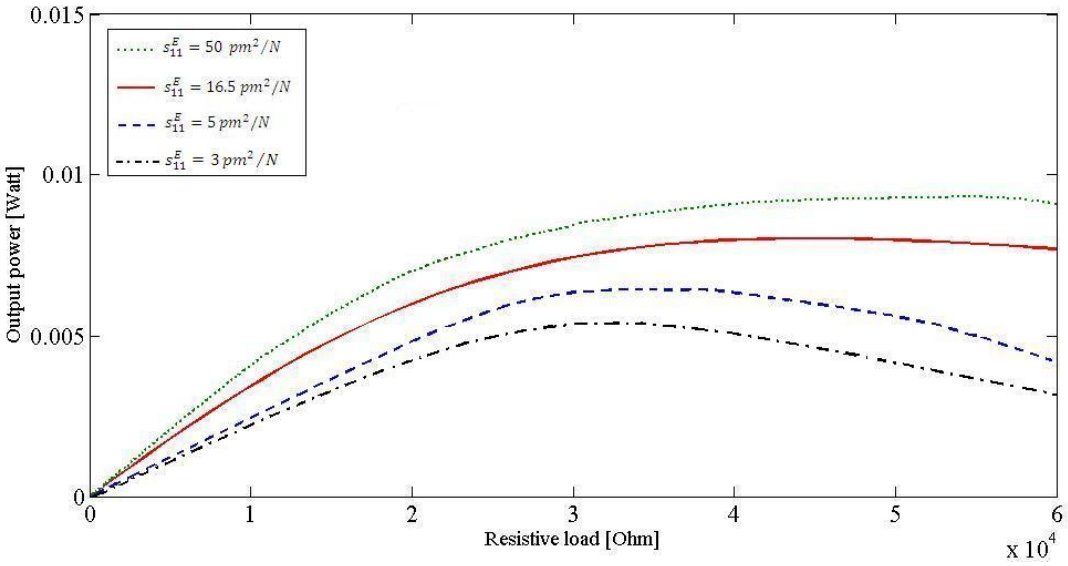

Fig. 4.6: Effect of the elastic compliance on the output power and the optimal load resistance

4.6.3. Effect of Relative Permittivity

In this case, the permittivity constant differs while the other parameters are the same. Thus, we choose a range of values for the relative permittivity to see its effect. Figure 4.7 shows that with the increase in the value of this constant, the output power slightly decreases.

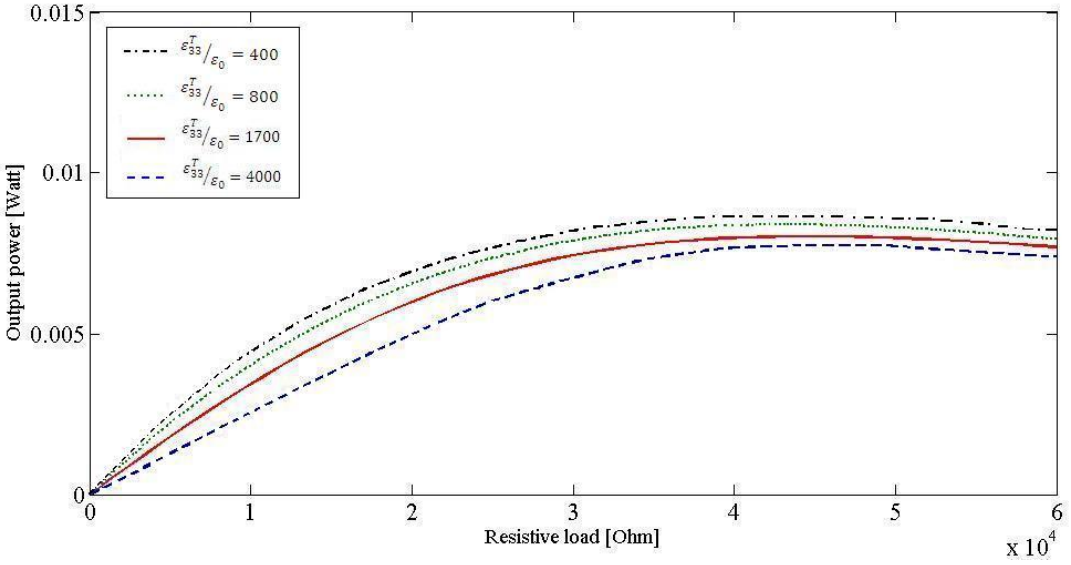

Fig. 4.7: Effect of the relative permittivity on the output power and the optimal load resistance

According to figure 4.7, the optimal load resistance of the harvester is not affected by the difference in the value of the relative permittivity. In addition to these parameters, as it was noted in section 4.4, the mechanical modal damping is another factor which is very effective in changing the optimal load resistance of the harvester.

4.6.4. Effect of the mechanical damping

As noted in section 4.4, the increase in the damping ratio causes an increase in the value of the optimal load resistance.

An important conclusion that can be drawn from the study of different parameters of the piezoelectric material is that the large value of piezoelectric constant does not have a significant effect on the output power independently, when other dynamic parameters and mechanical properties like damping are identical. Another important issue is that the output power of the system is more sensitive to the damping at the resonance frequency in comparison with other frequencies. In this study, the original damping ratio of the PZT used has been 1%. By changing this value to the value of 2% the calculations gives about 50% reduction in the value of output power at the resonance frequency.

As a result, having an energy harvester beam with less damping can be more effective than choosing piezoelectric materials with higher values of piezoelectric constant and the material properties that make higher values of output power. It should be noted that the damping ratio is not easy to predict and control in practice.

4.6.5. Tip mass Effect on the harvester dynamics

Figure 4.8 shows the effect of tip mass on the natural frequency of the energy harvester and the amplitude of the output voltage. As it is presented in section 4.3, with the increase in the value of tip mass, resonance frequency will decrease and the amplitude of voltage will increase.

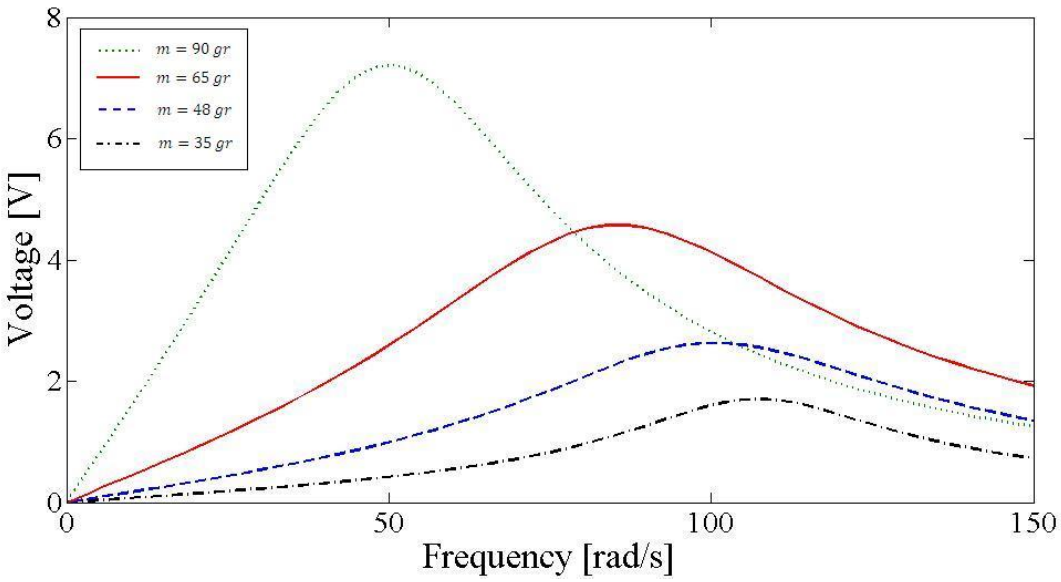

Fig. 4.8: Effect of the tip mass on the output voltage and the resonance frequency

Figure 4.8 shows the results of the study in which all parameters of the harvester are identical except tip mass value. Different values of 35 gr, 48 gr, 65 gr and 90 gr of tip mass have been selected for this study. It should be noted that due to the discussion in section 4.3, the effect of length of the beam on the natural frequency is the same (increase in the length of the beam causes decrease in the value of the natural frequency). Also the amplitude of vibrations have higher values with an increase in the length of the beam which finally causes higher amplitude of the output voltage.

CHAPTER 5:

NUMERICAL RESULTS, EXPERIMENTAL RESULTS AND MODEL VERIFICATION

Experimental setup and the fabricated prototype of the piezoelectric energy harvester are described in this chapter. Then the experimental validation of the single-mode analytical relationships is discussed. The experimentally measured voltage, optimal resistive load and the maximum power extracted from the harvester are compared with the numerical results from the closed form expressions derived in this paper. Effect of the tip mass on the natural frequency and amplitude of the output voltage is compared to what described in chapter 4. Tests are performed using two most common types of piezoelectric materials, PVDF and PZT. Test results for these two types are compared with each other at last.

5.1. Experimental setup for vibration energy harvesting from a rotating hub

The experimental setup for generating electric voltage from a rotating hub is shown in figure 5.1. Two different piezoelectric films are employed in our tests i.e. a

PZT manufactured by *MIDE Inc.* and a PVDF film manufactured by *Images SI, Inc.* (PZ-03). In this setup, a flexible cantilever beam is used and the piezoelectric film is bonded on it using sensor adhesive from *Loctite* (*Model No. 330*).

A tip mass is attached to the cantilever beam. The geometric and material properties of the piezoelectric layer and substructure are given in tables 5.1 and 5.2 for the PVDF harvester and tables 5.3 and 5.4 for the PZT harvester, respectively. The harvester is fastened rigidly on a cross hub as shown in the schematic diagram shown in figure 4.2. The hub is mounted on a shaft that is rotating with a constant speed. The cross hub has four places for fastening each energy harvester. Using four beams would increase the output power by four times; however, only one beam is used for validation of our model in this project.

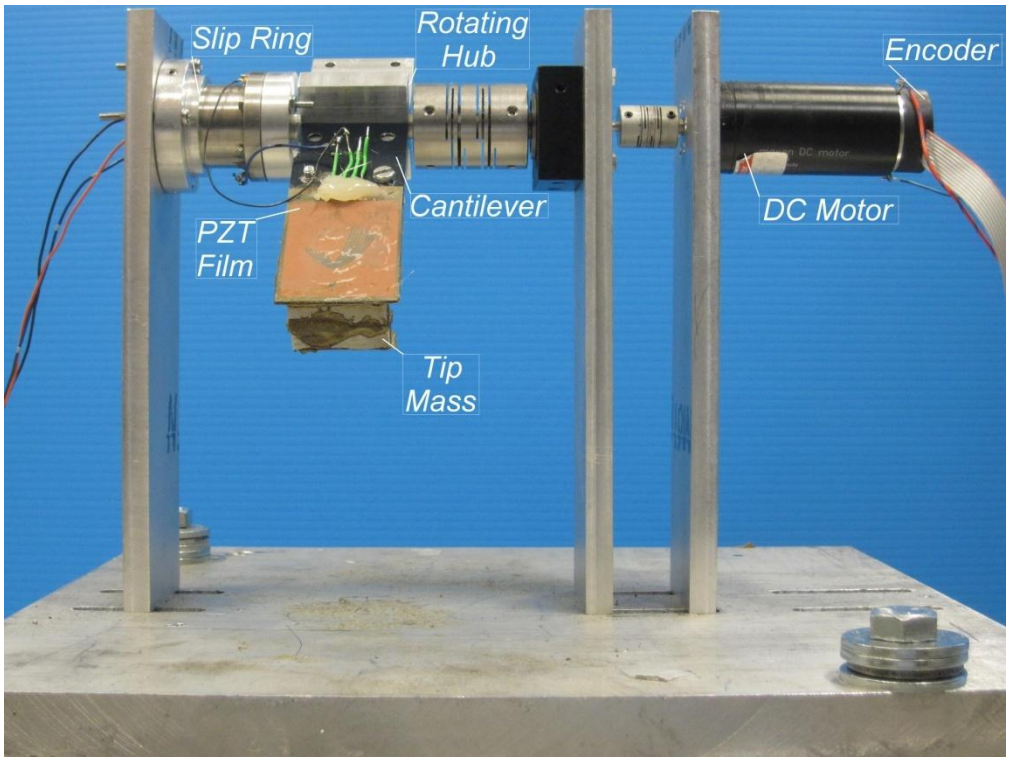

Fig.5.1: Experimental setup used for validating the analytical model

The shaft is driven by a DC motor from Maxon Motors (*A-max 32 Model No. 236669*) equipped with an encoder with 500 Counts per turn from Maxon Motors (*HEDL 5540 Model No. 110514*) for measuring the angular position of the shaft. The electric output voltage from the energy harvester and the encoder are both connected to a *Sensoray* 626 DAQ for measurement. To measure the electrical output of the system, the wires that are coming out from a slip ring are used. The slip ring is made by *Michigan Scientific Corp.* (S-series End of Shaft slip ring). Software interface which is used for this DAQ is Simulink. In figure 5.2, the Simulink block diagram for measuring the output of Encoder and output voltage of the harvester presented.

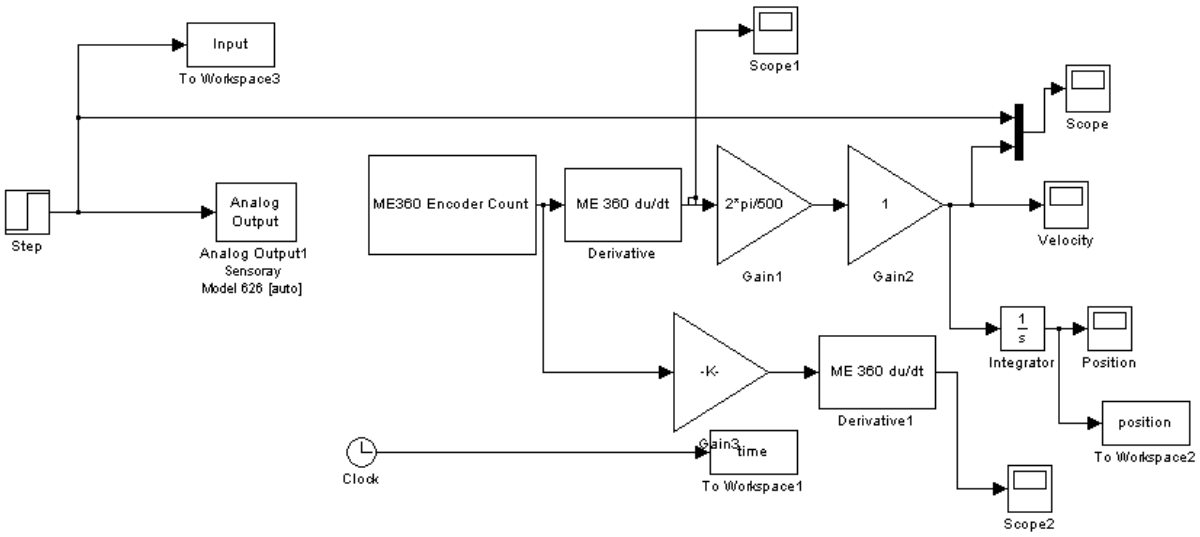

Fig. 5.2: Performing Data Acquisition in Simulink

This should be noted that the output of encoder is angular position. We use a derivative block to obtain angular speed. The gain block represents the gear ratio of the motor. Using this configuration the output of the system was measured with very negligible noise and the angular speed of the shaft was tracked easily and accurately.

In the experimental studies, the energy harvester was first tested with a non-optimal resistive load, i.e., a very low resistive load of 100 Ω. The output voltage was measured while the hub velocity (frequency of vibration of the beam) was swept. The maximum output voltage occurs at the natural frequency of the beam, which is monitored to identify the optimal hub rotational velocity. Using this hub velocity (natural frequency of the energy harvester), experiments were conducted by adjusting a variable resistance to obtain the optimum resistive load for which the output power is maximum. Then by setting the variable resistor on this optimal resistance, the output voltage of the harvester is measured while the hub velocity is swept.

Results for the power versus resistive load are shown in figures 5.5 and 5.6 for PVDF harvester. Then using the optimal value for the resistance, output voltage versus hub velocities (frequency) plotted. Figures 5.3 and 5.4 illustrate this plot for PVDF harvester. Tables 5.1 and 5.2 summarize the properties of the piezoelectric materials (PVDF) used in the experimental setup.

Table 5.1. Geometric parameters of the cantilever used for the experimental validation (PVDF harvester).

Geometric Parameters	PVDF	Substructure
Length, L (mm)	73	73
Width, b (mm)	16	16
Thickness, h (mm)	0.2	0.7
Tip mass (Kg)	0.065 &	0.048

Table 5.2. Material parameters of the cantilever used for the experimental validation (PVDF harvester).

Material Parameters	PVDF	Substructure
Mass Density, ρ (Kg.m^{-3})	1780	2700
Young's Modulus, Y (GPa)	4	70
Piezo. Constant, d_{31} (pmV^{-1})	23	–
Permittivity, ε_{33} (Fm^{-1})	$13\varepsilon_0$	–

5.2. Validation of the single-mode closed form expressions for the electric output

The mathematical model given by Eq. (4.41), (4.44) and (4.45) predict the output voltage, the optimal resistive load and the maximum power which can be extracted from the harvester. The modal damping ratio needed for the simulation is obtained experimentally from the exponential decay of the impact response of the beam. The damping ratio is measured for the two different masses where for 48 g and 65 g mass is 0.02 and 0.017, respectively. Eq. (4.39) and Eq. (4.40) suggest that the tip mass affects the natural frequency and voltage amplitude of the harvester. The output voltage of the harvester with the 600 kΩ resistive load is measured for 48 g and 65 g tip masses at different hub angular velocities as depicted in figures 5.3 and 5.4, respectively. The results indicate close agreement between the theory and experiments. Maximum error of the mathematical model occurs at the resonance frequency which is 8.6% for voltage response of PVDF harvester with 48 g tip mass and 5.8% for the harvester with 65 g tip mass when is compared with the experimental data.

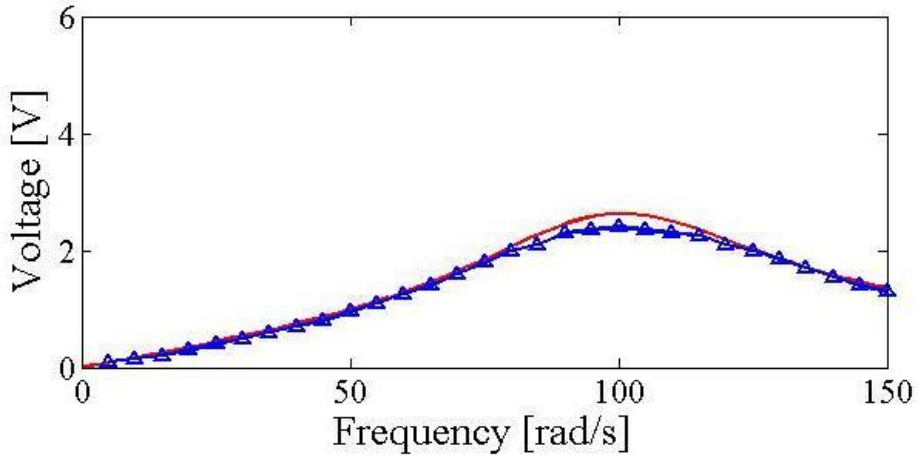

Fig.5.3: PVDF harvester Output voltage for 48 gram tip mass and R=600K, experimental data (blue dotted line) & theoretical data (red line)

The output power of the harvester was then calculated as given by Eq. (4.43). The calculated optimal load resistance for 48g and 65g tip masses are 560 and 540 kΩ, which are close to the case with 600 kΩ in our experiments with 6.7% and 10% error respectively.

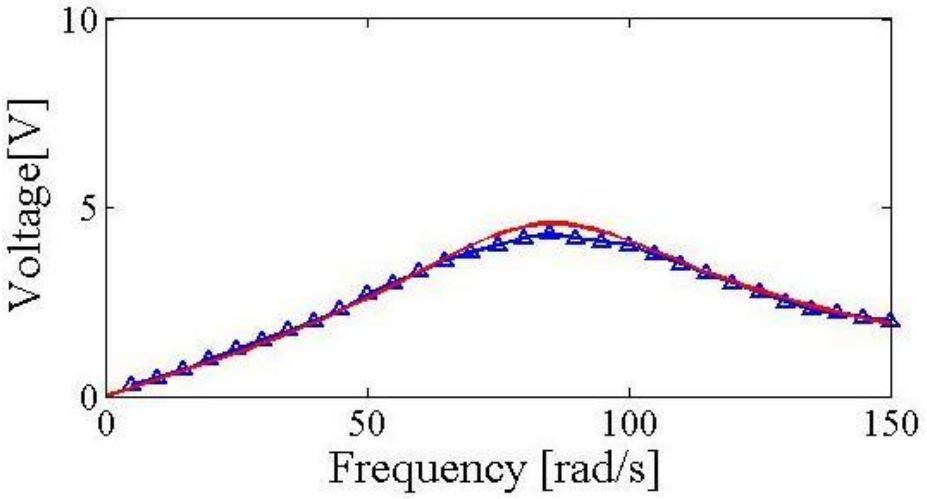

Fig.5.4: PVDF harvester Output voltage for 65 gram tip mass and R=600K, experimental data (blue dotted line) & theoretical data (red line)

Figures 5.5 and 5.6 illustrate the experimental and simulation results of the power versus resistive load when the PVDF transducer is used. The results illustrated in figures 5.5 and 5.6 indicate close agreement with experimental results. The output power value is calculated using the value of maximum voltage (voltage at resonance frequency) which contains the maximum error. Therefore, the output power is expected to have an almost constant error due to the systematic error occurred at this frequency. The experimental and simulation results indicate that the effect of tip mass on the optimum load resistance is negligible. Although the changes of tip mass intuitively alter the damping ratio, ζ, the value of viscous damping coefficient which is a characteristic of the system remains the same. The output power that was experimentally extracted from this device using the 65g tip mass at the optimal resistive load is 30.8 μW.

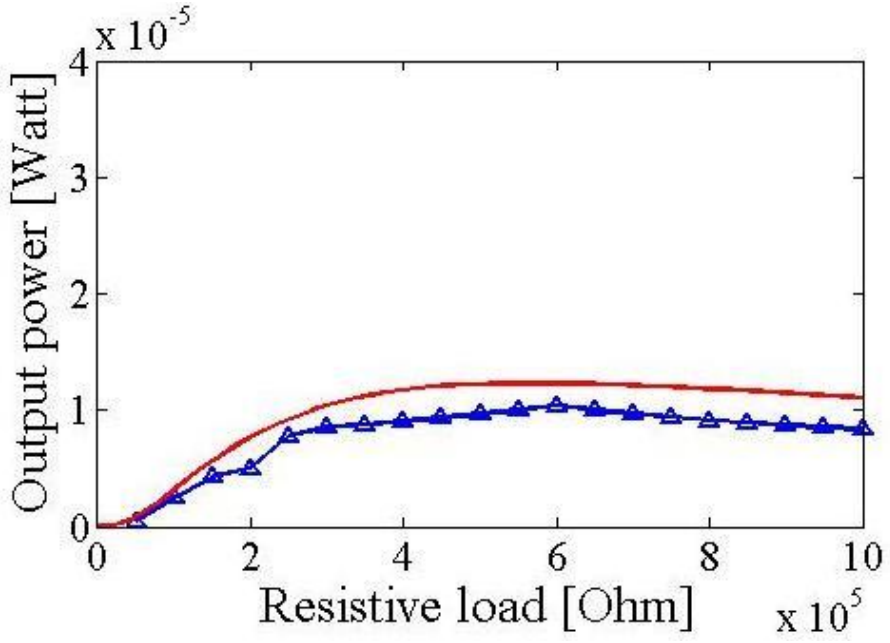

Fig. 5.5: PVDF harvester Output power versus resistive load for 48 gram tip mass, experimental data (blue dotted line) & theoretical data (red line)

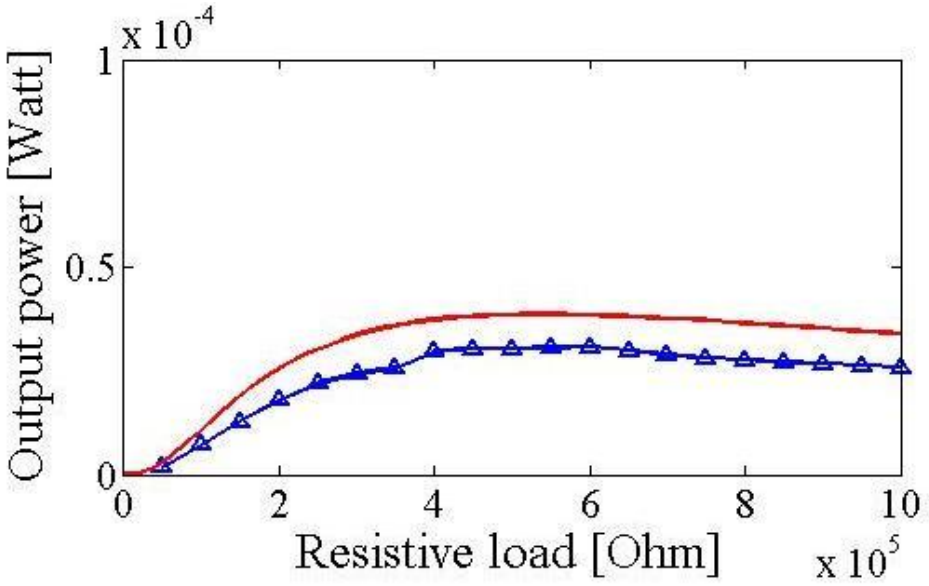

Fig. 5.6: PVDF harvester Output power versus resistive load for 65 gram tip mass, experimental data (blue dotted line) & theoretical data (red line)

The output power of the harvester with the 65g tip mass is higher than the harvester with 48g tip mass which generates 10.4 μW of power. Similar experiments were conducted for measuring the output voltage and calculating the optimal resistive load using the PZT layer. It should be noted that the PZT is a stiff material; thus increasing the natural frequency of the harvester beam. In the setup used for this experimental study, the angular velocity of the hub cannot reach velocities beyond 200 *rad/s* due to the maximum speed DC motor can reach. For tip mass values of 48 g and 65 g, the natural frequency will go beyond this limit. As a result, we had to reduce value of the natural frequency by increasing the tip mass or make the beam longer. We chose 105 g tip mass for performing the experiments.

The natural frequency of the harvester beam with this amount of tip mass is 138 *rad/s,* which is in the range of operation of the motor. To be able to compare the extracted power from the PVDF harvester and the PZT harvester, one should consider the similar physical conditions such as similar tip mass and similar length of the beam. The model which has been validated so far; indicates that the PVDF harvester with a 105 g tip mass generates the maximum output power of 147 μW when the harvester is connected to the optimal resistance. The amount of energy generated by this PVDF harvester is not enough to power most electronic devices [55].

Table 5.3. Geometric parameters of the cantilever used for the experimental validation (PZT harvester).

Geometric Parameters	PZT	Substructure
Length, L (mm)	50.8	50.8
Width, b (mm)	38.1	38.1
Thickness, h (mm)	0.13	0.5

Table 5.4. Material parameters of the cantilever used for the experimental validation (PZT harvester).

Material Parameters	PZT	Substructure
Young's Modulus, Y (GPa)	66	4.5
Piezo. Constant, d_{31} (pmV^{-1})	-190	–
Permittivity, ε_{33} (Fm^{-1})	$1700\varepsilon_0$	–

A simulation study was conducted for the new system based on the PZT harvester properties with the beam specifications summarized in tables 5.3 and 5.4. Again, the voltage versus hub velocity is measured using a non-optimal resistive load to obtain the natural frequency of the harvester. Then power versus the load resistance is measured at the natural frequency to find the optimal resistive load of the harvester. Finally using the optimal value for the resistive load, the output voltage through the optimal resistance of the harvester versus frequency is plotted by sweeping the rotational velocity of the hub. Figure 5.7 shows the experimental and theoretical results for the voltage output of the PZT energy harvester through an optimal load of 40KΩ which is obtained from the power versus load resistance plot. The maximum error in the voltage at the resonance frequency is 10.3% for the PZT harvester.

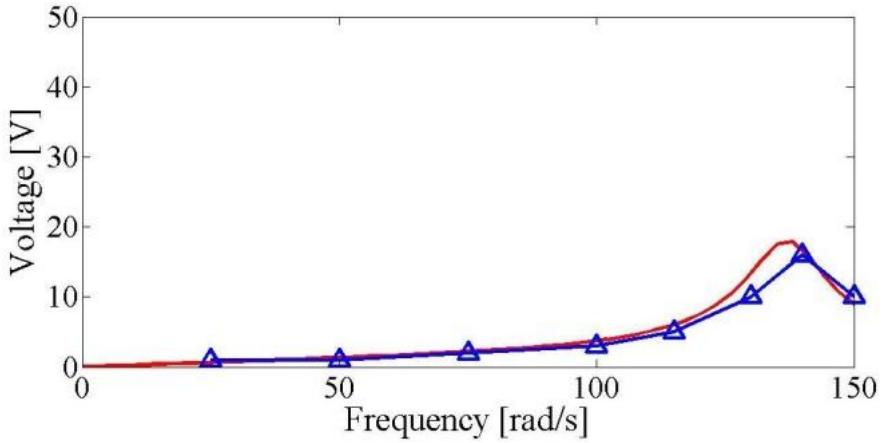

Fig.5.7: PZT harvester Output voltage, 105 gram tip mass and R=40K, experimental data (blue dotted line) & theoretical data (red line)

The output power versus resistive load is plotted for the PZT harvester in figure 5.8. Based on the experimental results, the maximum extracted power of PZT energy harvester occurred when the load resistance is 40 KΩ. This number matches to the resistive load calculated from the mathematical model. The experimentally measured maximum output power from the PZT energy harvester is 6.4 mW which is very close to the value calculated from Eq. (4.43). This amount of power is enough for supplying the wireless sensors after storing energy into an electrical storage media [55].

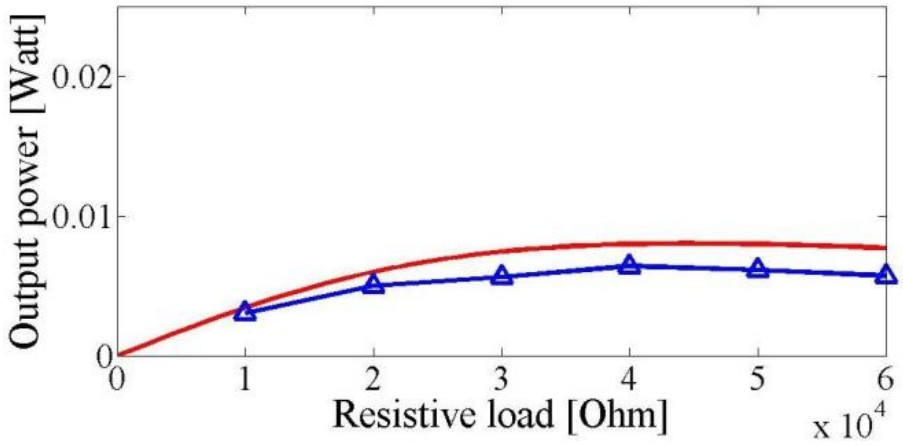

Fig. 5.8: PZT harvester Output power versus resistive load, 105 gram tip mass, experimental data (blue dotted line) & theoretical data (red line)

Comparing the results of the two harvesters investigated in this study reveals that PVDF has higher value of optimal resistive load than PZT (600KΩ in comparison with 40KΩ). The results show that the amplitude of generated power from the PZT harvester is about 44 times higher than PVDF (6.4 mW in comparison with 147 μW for the energy harvester beam with the same length and tip mass weight). This is in agreement with

previous findings that show the impedance of the designs (optimal load resistance) is higher for PVDF due to its very low dielectric constant and the maximum output power through the optimal load is much lower than PZT due to the drastically reduced coupling coefficient of PVDF [56].

CHAPTER 6: CONCLUSIONS AND RECOMMENDATIONS

In this thesis, the modeling and design of a piezoelectric vibration energy harvester was investigated. The piezoelectric energy harvester consists of a cantilever beam carrying a tip mass with the whole system mounted on a rotating horizontal hub. The proposed energy harvester has an inherent source of harmonic force due to the gravitational force of the tip mass. When the hub rotates with a constant angular velocity, the gravity force on the tip and its coupling with rotational motion causes the mass-beam system to vibrate. The focus of the project was on the development of a validated electromechanically coupled model of the cantilevered energy harvester. Analytical model that predicts power generation from the excited beam has been developed and examined. Distributed model of the cantilever beam has been developed based on the Euler-Bernoulli assumptions and assumed mode method. Separation of variables method has been employed to solve the partial differential equation. Using the boundary conditions of the system, mode shape is determined for different modes of vibration. Knowing the mode shape using Lagrangian approach, the equation of motion of the beam is derived. As the effect of piezoelectric transducer is added to the Lagrangian derivation, the equation of motion is coupled with voltage.

On the other side, the energy harvester is connected to a purely resistive load. The electrical circuit equation for the circuit is derived based on the Kirchhoff laws. The output current of the PZT sensor is function of strain and it makes the electrical governing equation coupled to the equation of motion. The purely resistive load which is used for this modelling is not being used in practice but it's a common practice to use it for modelling.

Damping of the beam is added to the equation of motion as it is measured experimentally from the exponential decay of the impulse response of the system. An important issue regarding this design is that the stiffness of the harvester varies with the change of the hub rotating speed. The increase in the rotating speed makes the beam less rigid by a factor proportional to the square of the speed.

Two electromechanical coupled governing equations of the system are solved using Laplace transform to derive closed form expressions for the vibration response, output voltage and output power of the energy harvester. Derivative of power with respect to time gives the optimal resistive load of the harvester after setting equal to zero. This optimal load maximizes the output power of the harvester.

Material parameters as well as geometrical characteristics such as tip mass and the length of the beam change the dynamics of the energy harvester. Damping is another parameter that changes dynamics of the energy harvester.

With a change in the value of piezoelectric constant, the optimum resistive load is affected; because this load depends on the electromechanical coupling; but the maximum power changed negligible. The decrease in the value of compliance constant causes the decrease in the value of optimal load resistance and the amplitude of power. With the increase in the value of relative permittivity, the output power slightly decreases but it doesn't affect the optimal resistive load of the harvester. Mechanical damping affects optimal load resistance and output power at the resonance frequency. Higher damping makes the value of optimal load higher and as a result the maximum output power decreases. Natural frequency of the energy harvester will be lower when the tip mass or length of the beam increases. Increase in the value of tip mass or length of the beam also makes the amplitude of output power increase.

Providing a test setup and data acquisition system, experimental results were performed to verify the mathematical model for predicting dynamic behaviour of the system. Materials used for tests are PZT and PVDF with the specifications described in chapter 5 of this thesis. Different tip masses have been provided to test with the PVDF harvester. Numerical analysis has been compared with the experimental results. As the results show very good match between theory and experiments; conclusively the model is validated and all predictions are correct. The output of the energy harvester is also shown that is enough for charging wireless sensors of health monitoring in rotary motion applications.

In summary, from the analysis performed the following contributions are made:

- An analytical model which uses the Euler-Bernoulli assumptions and assumed mode method to accurately predict voltage and power output from the harvester that is excited by a harmonic gravity force on the tip mass.
- The equation of motion developed in this research shows the stiffness term varies as the hub speed changes. In fact, the rotation makes the beam *less rigid* by a factor proportional to the square of the rotational speed. Influence of parameters for designing an efficient energy harvester is shown. Two main parameters that are considered are the tip mass and length of the beam.
- A study was performed to find the optimal resistive load for the harvester that makes the output power maximized. The effect of different parameters of the energy harvester on the value of this optimal load was evaluated. It was shown that how damping changes the optimal load value.
- Experiments for validation were performed for both PZT and PVDF. It was shown that the amplitude of extracted power from the PZT harvester is about 44 times higher than PVDF. So the PZT could be an attractive choice and the output power is sufficient to power the wireless sensors.

- Damping plays a critical role when predicting the generated power from piezoelectric energy harvester. Ideally, the damping ratio would be known to ensure accurate results. A way of determining the damping ratio involves performing log decrement analyses or frequency response calculations. It should be noted that the target of this research is to develop analytical model to reduce the need for experiments for predicting power harvested from a determined system.

From the experience of this work, the following recommendations on future work are suggested:

- An interactive, user-interface in the software code that would allow the user to input dimensions, parameters and properties of the system. This would allow easy use for someone who is not comfortable with coding and could remove possible input errors by directly changing the software code.
- In practice, the output voltage from the harvester is rectified and conditioned by the converter circuit for storing the harvested power in a storage media such as a large capacitor. However, the purely resistive electrical load gives a simple and useful way of calculating the power generated from the scavenger which has already been used in different models. The effects from the changes in the load can be explored in future.

- The storage of the generated power should be investigated. Storing a charge in a capacitor or recharging a battery are probable options.
- Applications for the use of the generated power were defined roughly. It can be determined with more details. For some applications the generated power may be low in magnitude, however can be used alternately if stored over time.

Appendix: Detail design and CAD drawings of the experimental setup

In this section, the detail design of each component of the proposed setup addressed; also Solidworks drawings presented. The first step to fabricate the rotating system is providing the rotating shaft that rotates around a horizontal axis. To reach this goal, a structure should be designed for holding the shaft in a specific height from the ground. Two walls are considered to hold the shaft. The shaft is then connected to a DC motor via a coupling. For selecting a DC motor, one should check out the maximum speed of the motor's shaft. To measure the rotational speed of the shaft, an encoder is employed to measure the angular position of the DC motor's shaft. The maxon motors company gives the opportunity of having a DC motor with an encoder attached to it. The serial number of the motor is *A-max 32 Model No. 236669* while the encoder is *HEDL 5540 Model No. 110514.* Motor itself should be kept above ground. For this purpose, another wall is considered. First the motor is going to be fastened by screws to a wall. Shaft of the motor is coming out of the wall. This shaft has a 4 mm dia. The main rotating shaft we designed is a 6 mm dia. So a coupling is needed for transforming these two dimensions. The idea for connecting these two shafts has been using another part that can be fixed to a wall. This part contains two shafts of 4mm and 6mm. The 4mm dia. Shaft is connected to the flexible coupling which is connected to the motor from its other side. The 6mm shaft of the part is going through the another coupling which is connected to the main shaft of 6mm dia. The four wings component as it is shown in Fig. 4.1 is fabricated with the holes for screwing the harvester on it. All the holes are threaded as it is safer than using nut and screw through the unthreaded holes. The shaft is connected to the slip ring from its other tip. For this reason, the shaft should contains a step for equating the diameter of that tip of the shaft and the slip ring diameter. Actually that is the rotating side of the slip ring which is connected to the shaft. The other side is fixed and screwed to another wall.

There is a relatively large hole in this wall for pulling out the wires of the slip ring. These three walls are finally screwed to a base plate. This base plate may be lifted during the test, especially in the resonance frequency, if it is light. For this reason, we attached the base plate to a very heavy component on the floor using large screws.

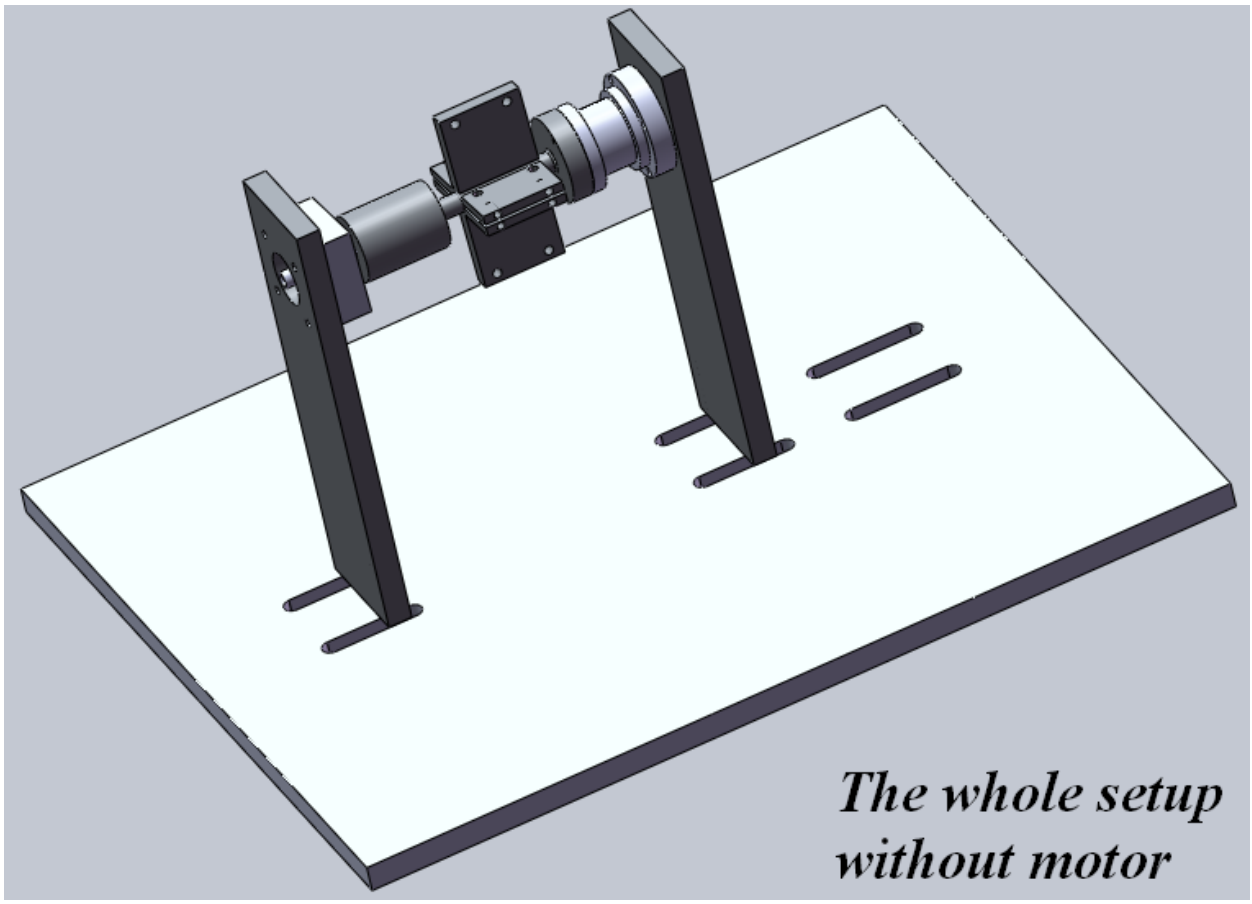

The followings are drawings for each component:

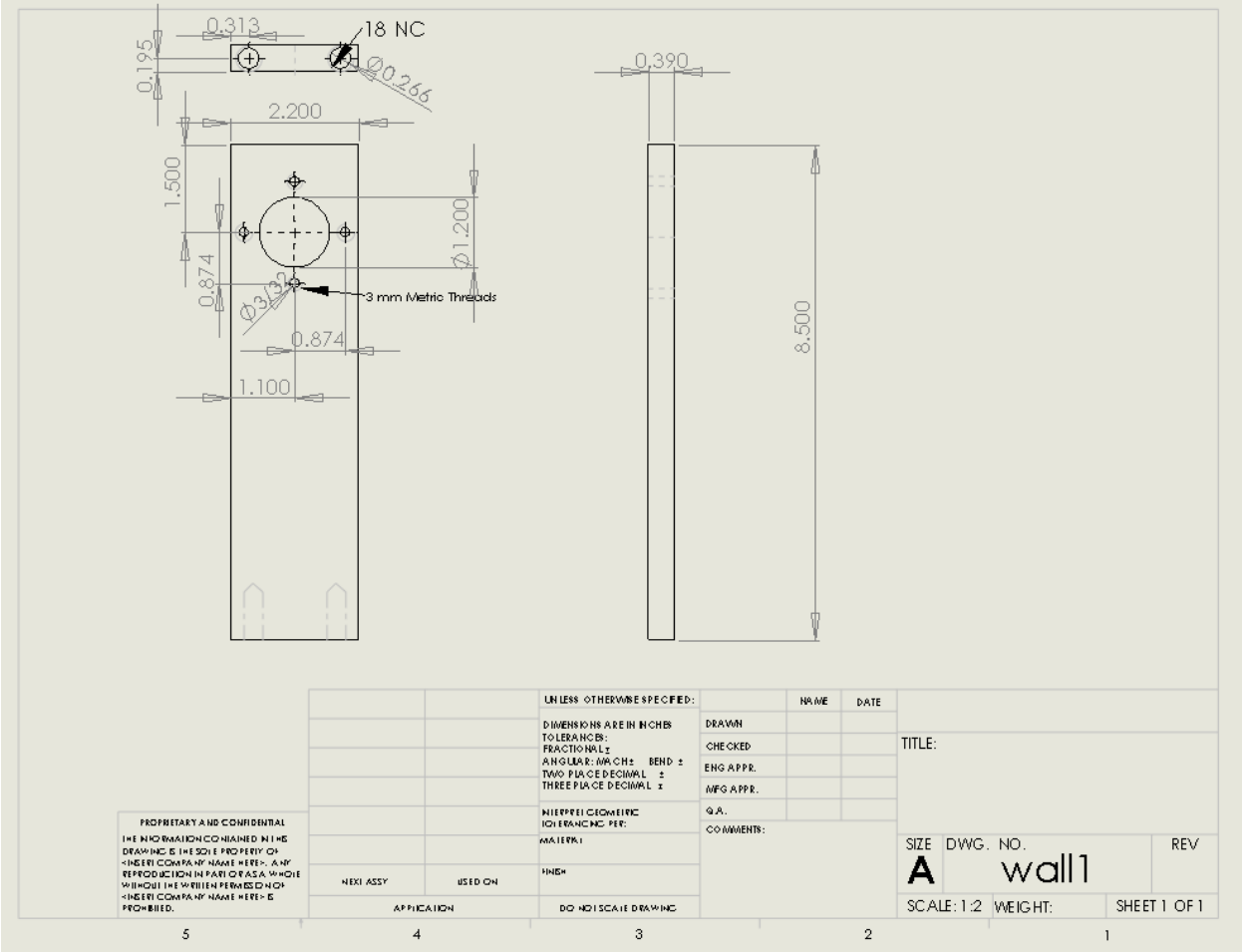
0.313
18 NC
0.195
Ø0.266
2.200
1.500
1.200
0.874
3 mm Metric Threads
0.874
1.100
0.390
8.500
UNLESS OTHERWISE SPECIFIED:
NAME
DATE
DIMENSIONS ARE IN INCHES
TOLERANCES:
FRACTIONAL ±
ANGULAR: MACH ± BEND ±
TWO PLACE DECIMAL ±
THREE PLACE DECIMAL ±
INTERPRET GEOMETRIC TOLERANCING PER:
MATERIAL
FINISH
DRAWN
CHECKED
ENG APPR.
MFG APPR.
Q.A.
COMMENTS:
TITLE:
SIZE
DWG. NO.
REV
A
wall1
SCALE: 1:2
WEIGHT:
SHEET 1 OF 1
NEXT ASSY
USED ON
APPLICATION
DO NOT SCALE DRAWING
PROPRIETARY AND CONFIDENTIAL
THE INFORMATION CONTAINED IN THE DRAWING IS THE SOLE PROPERTY OF <INSERT COMPANY NAME HERE>. ANY REPRODUCTION IN PART OR AS A WHOLE WITHOUT THE WRITTEN PERMISSION OF <INSERT COMPANY NAME HERE> IS PROHIBITED.
5
4
3
2
1

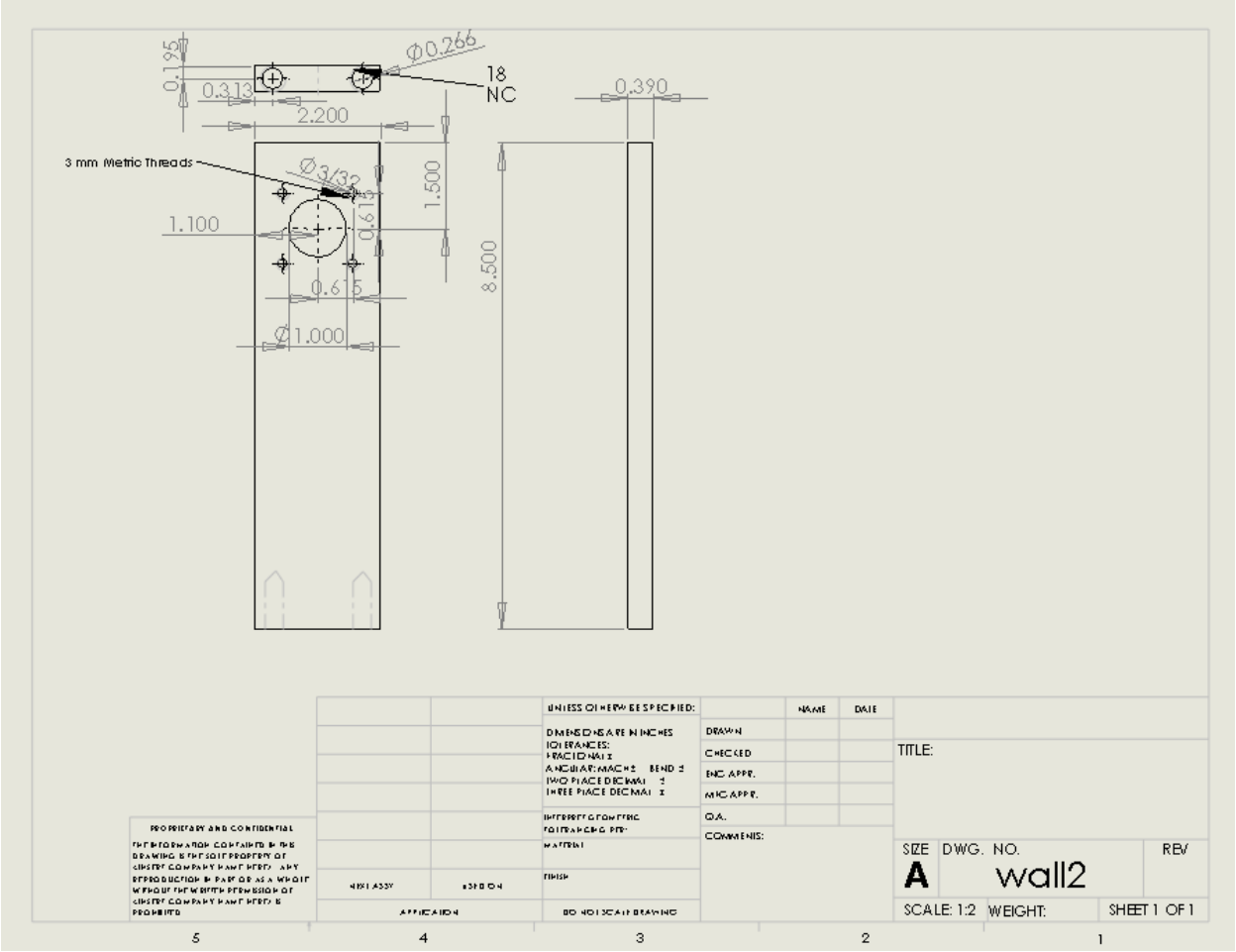
0.195
Ø0.266
18
NC
0.313
2.200
0.390
3 mm Metric Threads
Ø3/32
1.500
1.100
0.615
8.500
Ø1.000
UNLESS OTHERWISE SPECIFIED:
DIMENSIONS ARE IN INCHES
TOLERANCES:
FRACTIONAL ±
ANGULAR: MACH ± BEND ±
TWO PLACE DECIMAL ±
THREE PLACE DECIMAL ±
INTERPRET GEOMETRIC TOLERANCING PER:
MATERIAL
FINISH
DO NOT SCALE DRAWING
NAME
DATE
DRAWN
CHECKED
ENG APPR.
MFG APPR.
Q.A.
COMMENTS:
TITLE:
SIZE
A
DWG. NO.
wall2
REV
SCALE: 1:2
WEIGHT:
SHEET 1 OF 1
PROPRIETARY AND CONFIDENTIAL
THE INFORMATION CONTAINED IN THIS DRAWING IS THE SOLE PROPERTY OF <INSERT COMPANY NAME HERE>. ANY REPRODUCTION IN PART OR AS A WHOLE WITHOUT THE WRITTEN PERMISSION OF <INSERT COMPANY NAME HERE> IS PROHIBITED
NEXT ASSY
USED ON
APPLICATION
5
4
3
2
1

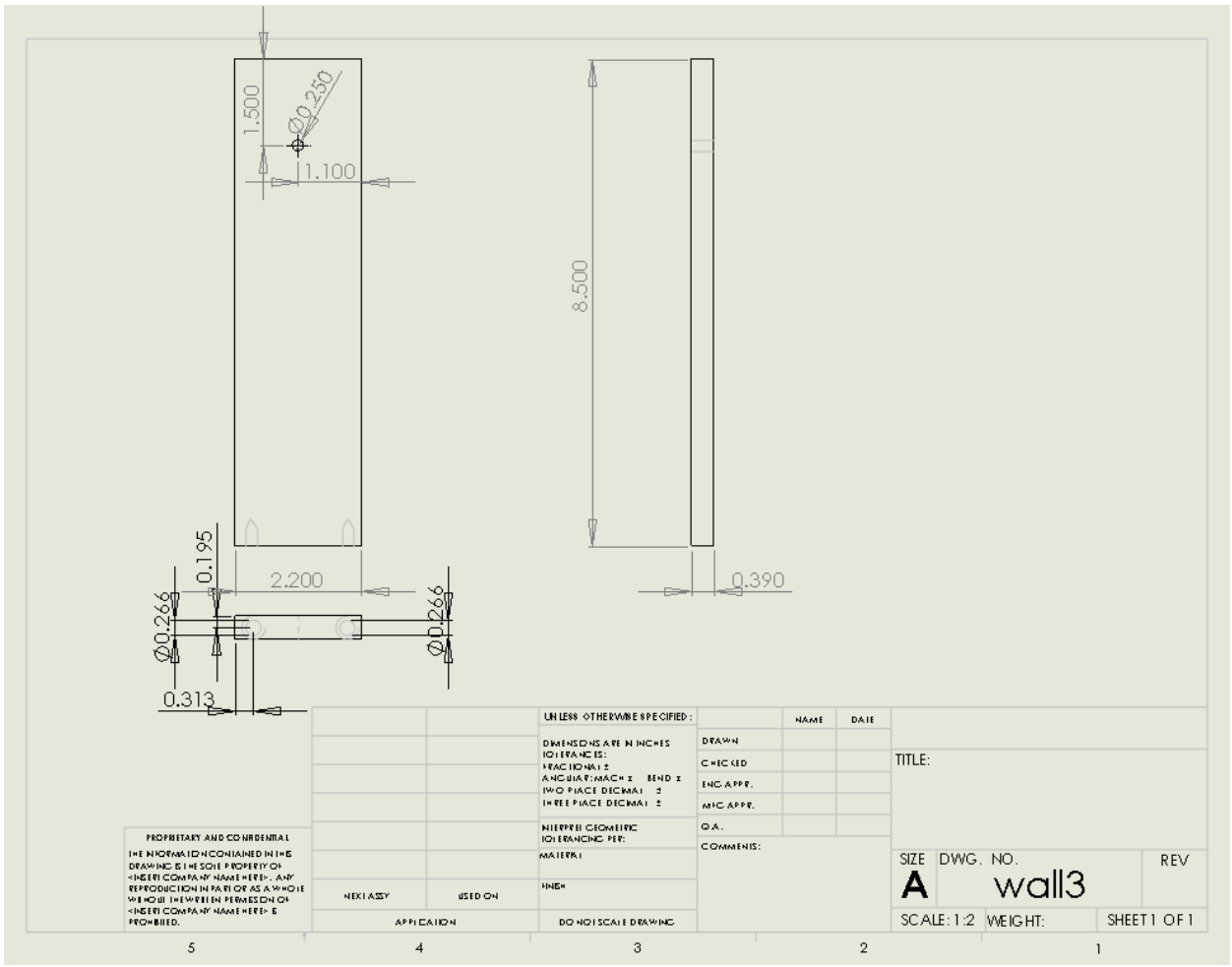
1.500
Ø0.250
1.100
8.500
0.195
2.200
0.390
Ø0.266
Ø0.266
0.313
UNLESS OTHERWISE SPECIFIED:
DIMENSIONS ARE IN INCHES
TOLERANCES:
FRACTIONAL ±
ANGULAR: MACH ± BEND ±
TWO PLACE DECIMAL ±
THREE PLACE DECIMAL ±
INTERPRET GEOMETRIC TOLERANCING PER:
MATERIAL
FINISH
NEXT ASSY
USED ON
APPLICATION
DO NOT SCALE DRAWING
NAME
DATE
DRAWN
CHECKED
ENG APPR.
MFG APPR.
Q.A.
COMMENTS:
TITLE:
SIZE
A
DWG. NO.
wall3
REV
SCALE: 1:2
WEIGHT:
SHEET 1 OF 1
PROPRIETARY AND CONFIDENTIAL
THE INFORMATION CONTAINED IN THIS DRAWING IS THE SOLE PROPERTY OF <INSERT COMPANY NAME HERE>. ANY REPRODUCTION IN PART OR AS A WHOLE WITHOUT THE WRITTEN PERMISSION OF <INSERT COMPANY NAME HERE> IS PROHIBITED.
5
4
3
2
1

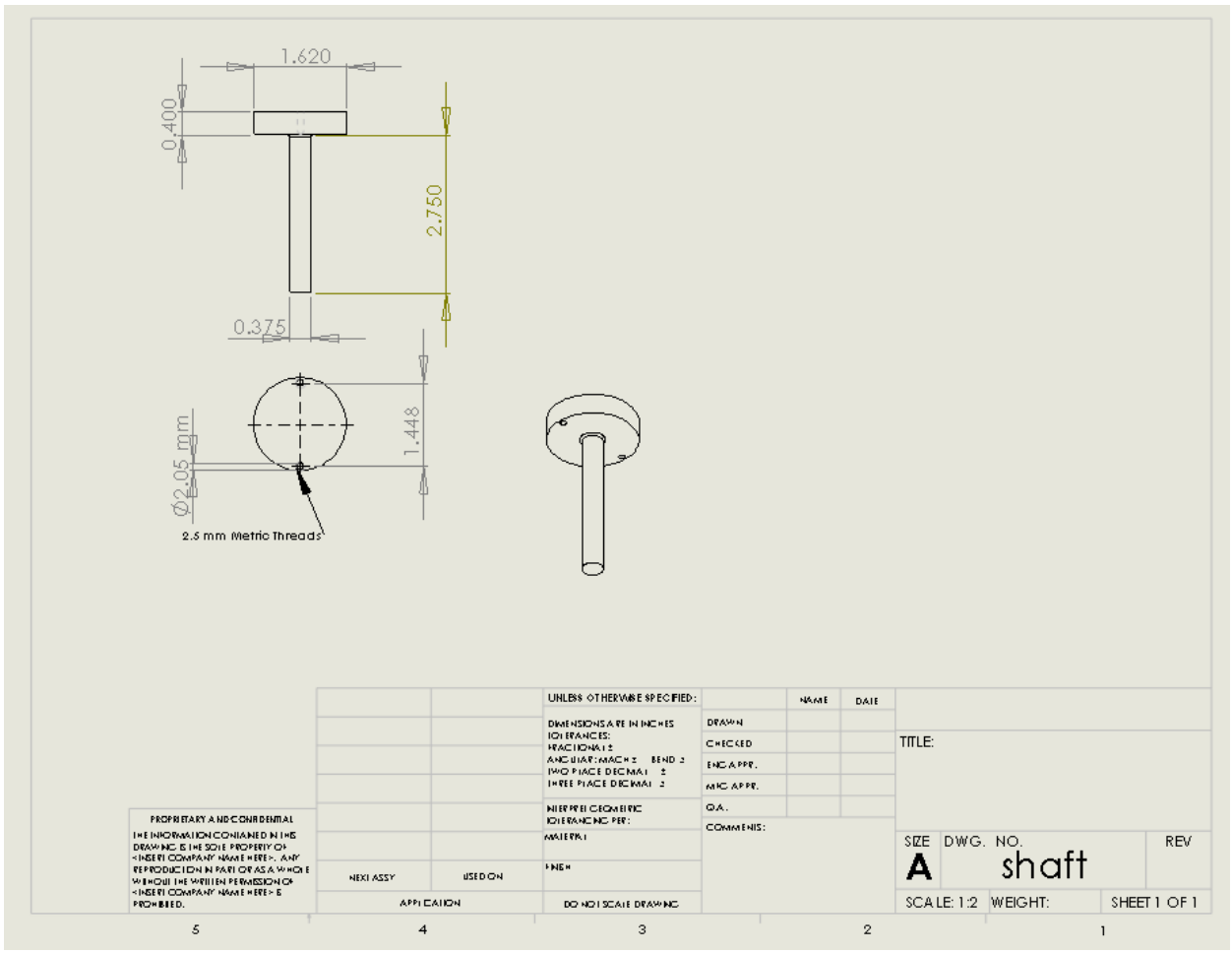
1.620
0.400
2.750
0.375
1.448
Ø2.05 mm
2.5 mm Metric Threads
UNLESS OTHERWISE SPECIFIED:
NAME
DATE
DRAWN
CHECKED
ENG APPR.
MFG APPR.
Q.A.
COMMENTS:
TITLE:
SIZE
A
DWG. NO.
shaft
REV
SCALE: 1:2
WEIGHT:
SHEET 1 OF 1
NEXT ASSY
USED ON
APPLICATION
DO NOT SCALE DRAWING
PROPRIETARY AND CONFIDENTIAL
5
4
3
2
1

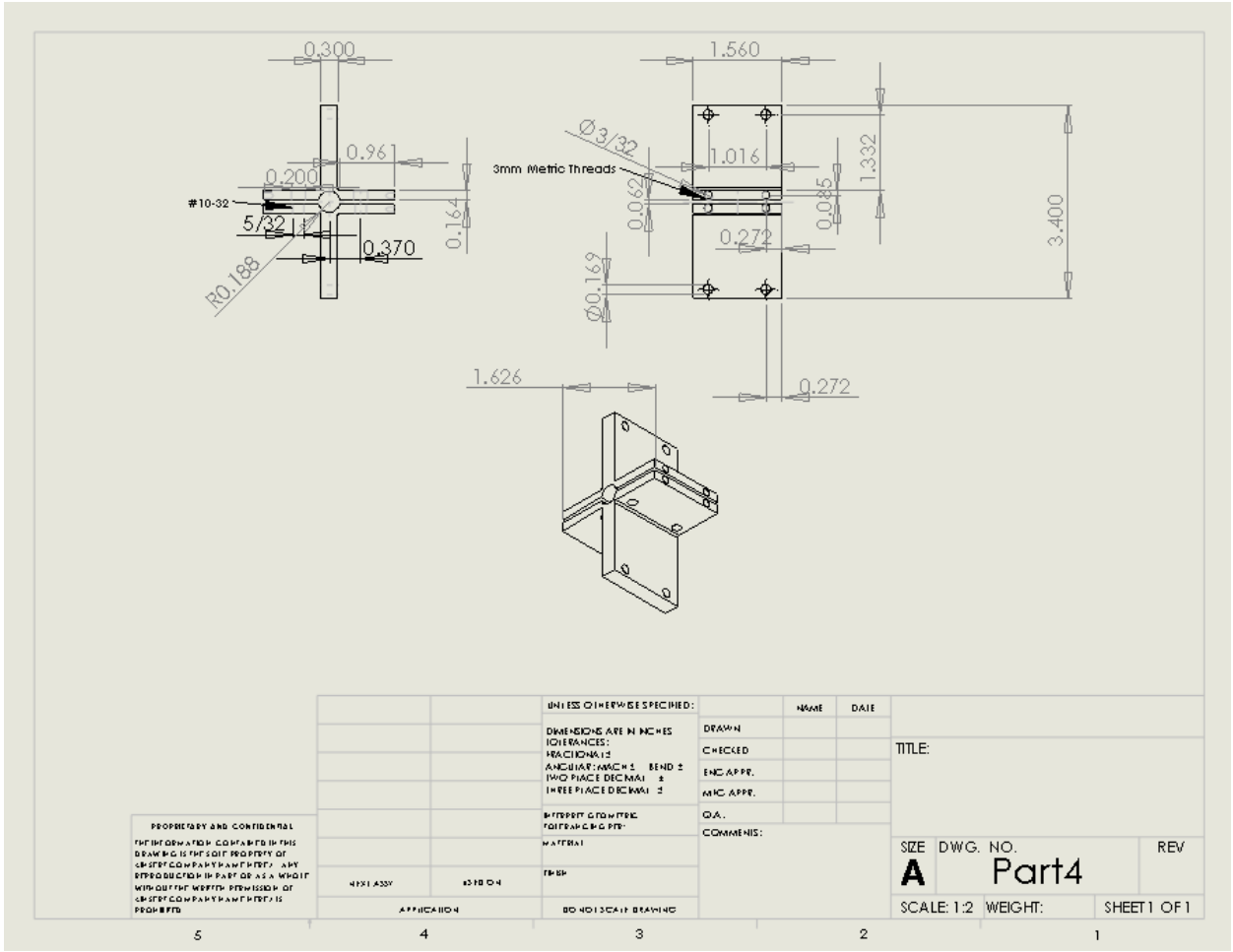
0.300
0.96
0.200
#10-32
5/32
0.370
0.164
R0.188
1.560
Ø3/32
3mm Metric Threads
1.016
1.332
0.062
0.085
3.400
0.272
Ø0.169
1.626
0.272
UNLESS OTHERWISE SPECIFIED:
DIMENSIONS ARE IN INCHES
TOLERANCES:
FRACTIONAL ±
ANGULAR: MACH ± BEND ±
TWO PLACE DECIMAL ±
THREE PLACE DECIMAL ±
INTERPRET GEOMETRIC TOLERANCING PER:
MATERIAL
FINISH
NEXT ASSY
USED ON
APPLICATION
DO NOT SCALE DRAWING
NAME
DATE
DRAWN
CHECKED
ENG APPR.
MFG APPR.
Q.A.
COMMENTS:
TITLE:
PROPRIETARY AND CONFIDENTIAL
THE INFORMATION CONTAINED IN THIS DRAWING IS THE SOLE PROPERTY OF <INSERT COMPANY NAME HERE>. ANY REPRODUCTION IN PART OR AS A WHOLE WITHOUT THE WRITTEN PERMISSION OF <INSERT COMPANY NAME HERE> IS PROHIBITED
SIZE
A
DWG. NO.
Part4
REV
SCALE: 1:2
WEIGHT:
SHEET 1 OF 1
5
4
3
2
1

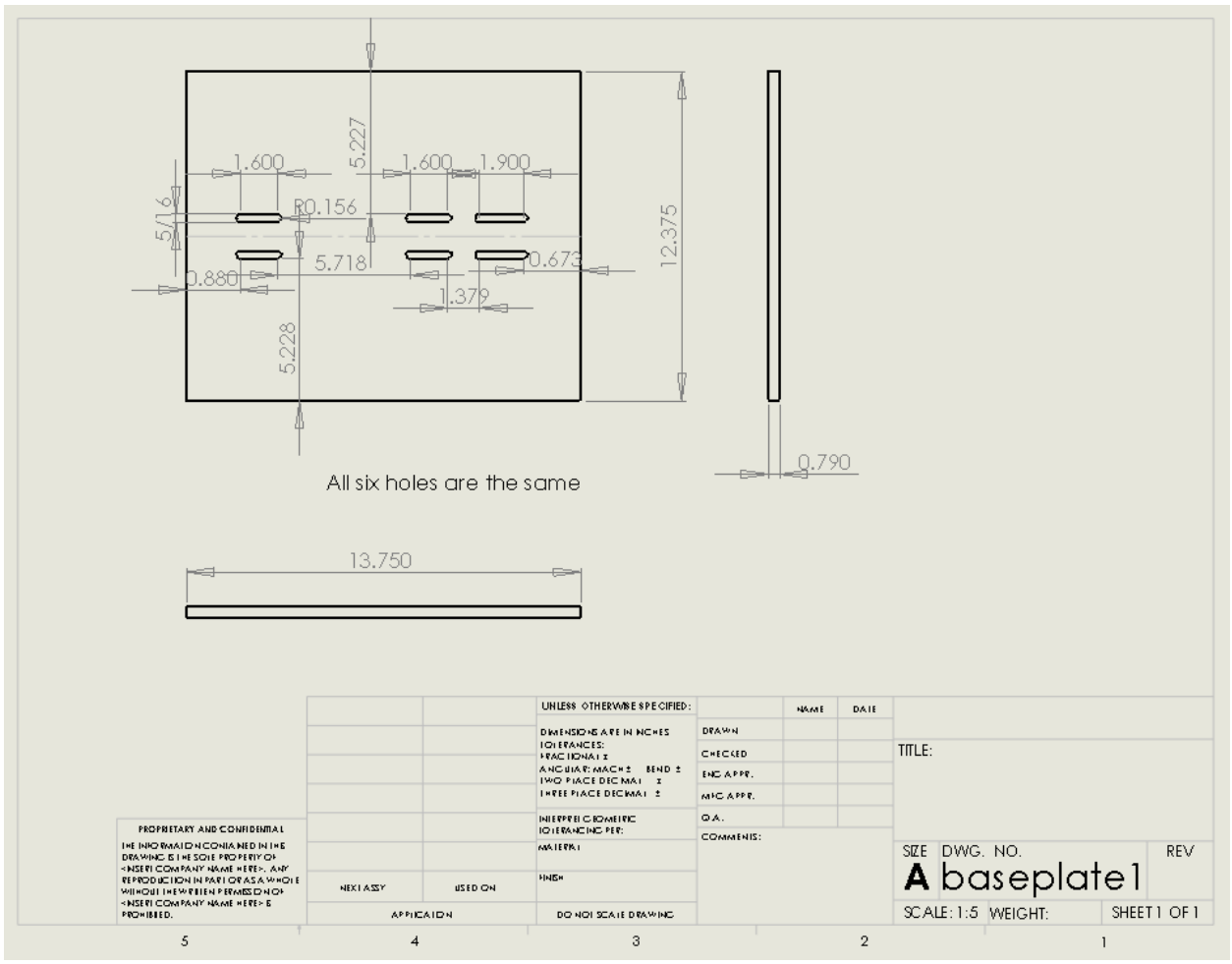
1.600
5.227
1.600
1.900
5/16
R0.156
12.375
5.718
0.673
0.880
1.379
5.228
0.790
All six holes are the same
13.750
UNLESS OTHERWISE SPECIFIED:
DIMENSIONS ARE IN INCHES
TOLERANCES:
FRACTIONAL ±
ANGULAR: MACH ± BEND ±
TWO PLACE DECIMAL ±
THREE PLACE DECIMAL ±
INTERPRET GEOMETRIC TOLERANCING PER:
MATERIAL
FINISH
NEXT ASSY
USED ON
APPLICATION
DO NOT SCALE DRAWING
NAME
DATE
DRAWN
CHECKED
ENG APPR.
MFG APPR.
Q.A.
COMMENTS:
TITLE:
SIZE
DWG. NO.
REV
A baseplate1
SCALE: 1:5
WEIGHT:
SHEET 1 OF 1
PROPRIETARY AND CONFIDENTIAL
THE INFORMATION CONTAINED IN THE DRAWING IS THE SOLE PROPERTY OF <INSERT COMPANY NAME HERE>. ANY REPRODUCTION IN PART OR AS A WHOLE WITHOUT THE WRITTEN PERMISSION OF <INSERT COMPANY NAME HERE> IS PROHIBITED.
5
4
3
2
1

Drawings pertain to the fabricated parts. For connecting the main rotating shaft to the shaft of the DC motor, two flexible couplings are utilized which have been purchased from SDP/SI company with the catalogue number S50MST-S06P37P37 and S50MSTMA16P04P04. They have the following specifications:

Inch Inch Inch Inch Inch Inch Inch Inch Inch

SDP/SI

Slit Type MST Flexible Couplings

Stock Drive Products/Sterling Instrument ■ **Phone: 516-326-3300** ■ **Fax: 516-326-8827**

■ **ZERO BACKLASH** ■ **SET SCREW TYPE** ■ **HIGH TORSIONAL STIFFNESS**

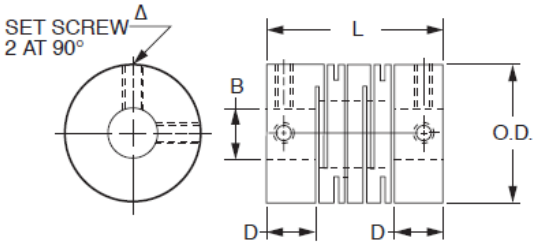

MISALIGNMENT COMPENSATION
Max. Angular Offset – 2°

MATERIAL: Stainless Steel

Catalog Number	O.D.	B* Bore	L Length	D	Set Δ Screw	Max.** Bore
Δ **S50MST-S01P12P12**	.315	.1250	.551	.138	#2–56	.1575
S50MST-S02P18P18	.472	.1875	.728	.197	#4–40	.2362
S50MST-S03P25P25	.630	.2500	.906	.256	#4–40	.3150
S50MST-S04P25P25	.787	.2500	1.024	.295	#4–40	.3937
S50MST-S04P37P37	.787	.3750	1.024	.295	#4–40	.3937
S50MST-S05P25P25	.984	.2500	1.220	.335	#6–32	.4724
S50MST-S05P37P37	.984	.3750	1.220	.335	#6–32	.4724

*Bore Tolerance: .1250 & .1875 $^{+.0007}_{-.0000}$
.2500 & .3750 $^{+.0009}_{-.0000}$

**Other bore diameter combinations and bore sizes not exceeding the maximum listed above are available on special order.

ΔCouplings with bore diameters **B** of .1575 or less have one set screw at each end.

SPECIFICATIONS

Coupling Series (Ref. only)	Rated Torque lb. in.	Max. rpm	Moment of Inertia ΔΔ oz. in²	Static Torsional Stiffness lb. in. / deg	Max. Lateral Offset	Max. Axial Motion	Weight ΔΔ oz.
S50MST-S01P...	1.77	78000	1.7×10^{-3}	7.724	.004	±.008	.11
S50MST-S02P...	2.66	52000	1.1×10^{-2}	9.886	.004	±.012	.33
S50MST-S03P...	4.43	39000	4.6×10^{-2}	13.130	.004	±.012	.74
S50MST-S04P...	8.85	31000	1.3×10^{-1}	38.619	.004	±.012	1.34
S50MST-S05P...	17.70	25000	3.7×10^{-1}	50.977	.006	±.016	2.51

ΔΔBased on Max. Bore.

Continued on the next page

Slit Type MST Flexible Couplings

SDP/SI
Stock Drive Products/Sterling Instrument ■ Phone: 516-328-3300 ■ Fax: 516-326-8827

■ ZERO BACKLASH ■ SET SCREW TYPE ■ HIGH TORSIONAL STIFFNESS

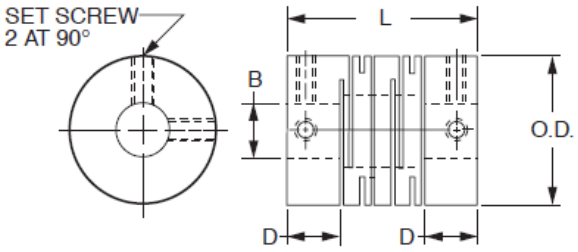

MISALIGNMENT COMPENSATION
Max. Angular Offset – 2°
Max. Axial Motion – ± .02

MATERIAL: Stainless Steel

Catalog Number	O.D.	B* Bore	L Length	D	Set Screw	Max.** Bore
S50MST-S06P37P37 S50MST-S06P50P50	1.26	.3750 .5000	1.61	.472	#6–32	.6299
S50MST-S07P50P50 S50MST-S07P62P62	1.57	.5000 .6250	2.20	.669	#10–24	.7874
S50MST-S08P50P50 S50MST-S08P62P62	1.97	.5000 .6250	2.80	.827	1/4–20	.9843
S50MST-S09P62P62 S50MST-S09P75P75	2.48	.6250 .7500	3.54	1.024	5/16–18	1.3780

*Bore Tolerance: .3750 $^{+.0009}_{-.0000}$
.5000 & .6250 $^{+.0011}_{-.0000}$
.7500 $^{+.0013}_{-.0000}$

**Other bore diameter combinations and bore sizes not exceeding the maximum listed above are available on special order.

SPECIFICATIONS

Coupling Series (Ref. only)	Rated Torque lb. in.	Max. rpm	Moment of Inertia$^{\Delta}$ oz. in^2	Static Torsional Stiffness lb. in. / deg	Max. Lateral Offset	Weight$^{\Delta}$ oz.
S50MST-S06P...	30.98	19000	1.421	131.30	.006	5.65
S50MST-S07P...	70.81	15000	4.756	154.48	.008	12.36
S50MST-S08P...	132.76	12000	14.761	216.27	.008	24.71
S50MST-S09P...	309.78	10000	45.923	278.06	.008	45.89

$^{\Delta}$Based on Max. Bore.

NEW SIZES

Miniature Slit Type Flexible Couplings

SDP/SI
Stock Drive Products/Sterling Instrument ■ Phone: 516-328-3300 ■ Fax: 516-326-8827

■ ZERO BACKLASH ■ SET SCREW TYPE ■ HIGH TORSIONAL STIFFNESS

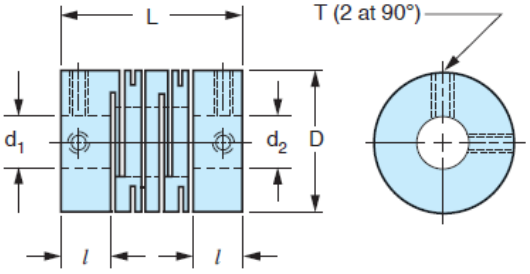

The projections shown are per ISO convention.

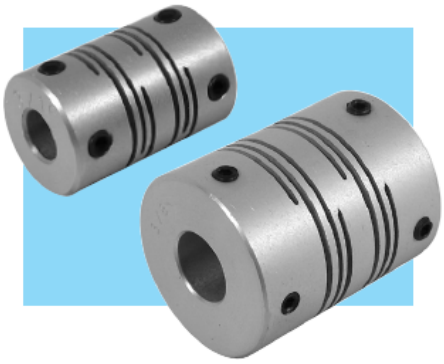

Continued on the next page

MISALIGNMENT COMPENSATION
Max. Angular Offset – 2°

MATERIAL: Anodized Aluminum

Catalog Number	D	d_1* Bore H8	d_2* Bore H8	L	*l*	T Set Screw	Max.** Bore
S50MSTMA08P02P02	8	2	2	14	3.5	M2Δ	4
S50MSTMA08P02P03		2	3				
S50MSTMA08P03P03		3	3				
S50MSTMA12P03P03	12	3	3	18.5	5	M2.5Δ	6
S50MSTMA12P04P04		4	4				
S50MSTMA12P05P05		5	5				
S50MSTMA16P04P04	16	4	4	23	6.5	M3Δ	8
S50MSTMA16P04P06		4	6				
S50MSTMA16P06P06		6	6				
S50MSTMA20P06P06	20	6	6	26	7.5	M3	10
S50MSTMA20P06P08		6	8				
S50MSTMA20P08P08		8	8				
S50MSTMA25P08P08	25	8	8	31	8.5	M4	12
S50MSTMA25P08P10		8	10				
S50MSTMA25P10P10		10	10				

*Bore Tolerance: 2 & 3 mm +0.014
4, 5 & 6 mm +0.018
8 & 10 mm +0.022

**Other bore diameter combinations and bore sizes not exceeding the maximum listed above are available on special order.

ΔCouplings with a bore diameter of 4 mm or less have one set screw in each hub.

SPECIFICATIONS

Coupling Series (Ref. only)	Rated Torque N•m	Max. rpm	Moment of InertiaΔΔ kg•m²	Static Torsional Stiffness N•m/rad	Max. Lateral Offset	Max. Axial Motion	WeightΔΔ grams
S50MSTMA08...	0.1	78000	1.2×10^{-8}	25	0.1	± 0.2	1.4
S50MSTMA12...	0.4	52000	8.3×10^{-8}	45	0.1	± 0.3	3.7
S50MSTMA16...	0.5	39000	3.3×10^{-7}	80	0.1	± 0.4	8.1
S50MSTMA20...	1	31000	9×10^{-7}	170	0.1	± 0.4	14
S50MSTMA25...	2	25000	2.6×10^{-6}	380	0.15	± 0.5	27

ΔΔBased on max. bore dimension.

Specifications of the motor and encoder are shown in the following.

A-max 32 ∅32 mm, Graphite Brushes, 20 Watt

HighPower

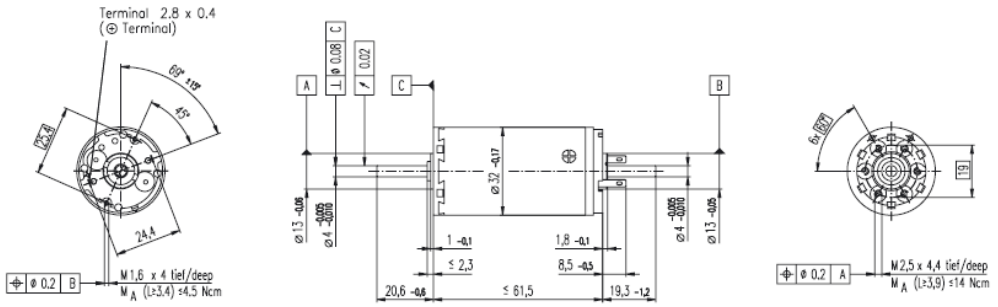

M 1:2

Stock program
Standard program
Special program (on request!)

	Motor Data		Order Number 236666	236667	236668	236669	236670	236671	236672
1	Assigned power rating	W	20	20	20	20	20	20	20
2	Nominal voltage	Volt	6.0	9.0	12.0	24.0	30.0	36.0	42.0
3	No load speed	rpm	4780	4920	4610	6420	6130	5820	5620
4	Stall torque	mNm	121	130	131	206	194	187	178
5	Speed / torque gradient	rpm / mNm	41.0	39.0	36.0	31.7	32.1	31.6	32.1
6	No load current	mA	242	165	115	81	62	49	40
7	Starting current	mA	10500	7670	5430	5860	4220	3220	2530
8	Terminal resistance	Ohm	0.573	1.17	2.21	4.09	7.11	11.2	16.6
9	Max. permissible speed	rpm	6000	6000	6000	6000	6000	6000	6000
10	Max. continuous current	mA	3610	2520	1840	1350	1020	817	671
11	Max. continuous torque	mNm	41.7	42.7	44.5	47.3	47.1	47.5	47.1
12	Max. power output at nominal voltage	mW	14100	16000	15300	33900	30500	28000	25700
13	Max. efficiency	%	69	71	72	77	77	77	76
14	Torque constant	mNm / A	11.5	17.0	24.2	35.1	46.0	58.1	70.2
15	Speed constant	rpm / V	827	563	394	272	208	164	136
16	Mechanical time constant	ms	18	16	15	14	14	14	14
17	Rotor inertia	gcm²	42.4	39.0	39.7	43.0	41.9	42.2	41.3
18	Terminal inductance	mH	0.06	0.13	0.26	0.55	0.95	1.52	2.21
19	Thermal resistance housing-ambient	K / W	7.5	7.5	7.5	7.5	7.5	7.5	7.5
20	Thermal resistance rotor-housing	K / W	2.1	2.1	2.1	2.1	2.1	2.1	2.1
21	Thermal time constant winding	s	17	16	16	17	17	17	17

Specifications

- Axial play 0.12 - 0.22 mm
- Max. **ball bearing** loads
  axial (dynamic) 7.6 N
  radial (5 mm from flange) 32.0 N
  Force for press fits (static) 110 N
  (static, shaft supported) 2000 N
- Max. **sleeve bearing** loads
  axial (dynamic) 5 N
  radial (5 mm from flange) 10.5 N
  Force for press fits (static) 110 N
  (static, shaft supported) 2000 N
- Radial play **ball bearing** 0.025 mm
- Radial play **sleeve bearing** 0.012 mm
- Ambient temperature range -20 ... +85°C
- Max. rotor temperature +125°C
- Number of commutator segments 13
- Weight of motor 242 g
- 2 pole permanent magnet
- Values listed in the table are nominal.
  For applicable tolerances see page 43.
  For additional details please use the maxon selection program on the enclosed CD-ROM.
- Options: Sleeve bearings in place of ball bearings and pigtails in place of terminals.

Operating Range

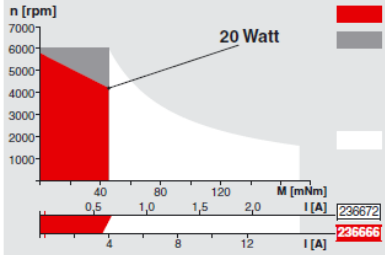

Comments

Details on page 49

Recommended operating range

Continuous operation
In observation of above listed thermal resistances (lines 19 and 20) the maximum permissible rotor temperature will be reached during continuous operation at 25°C ambient.
= Thermal limit.

Short term operation
The motor may be briefly overloaded (recurring).

236672 Motor with high resistance winding
236666 Motor with low resistance winding

maxon Modular System

Overview on page 17 - 21

Planetary Gearhead
∅32 mm
0.75 - 4.5 Nm
Details page 219

Planetary Gearhead
∅32 mm
1.0 - 6.0 Nm
Details page 221

Spur Gearhead
∅38 mm
0.1 - 0.6 Nm
Details page 223

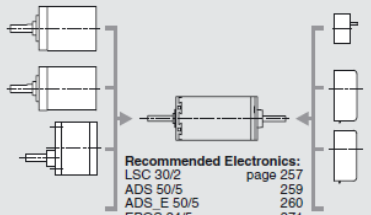

Recommended Electronics:

LSC 30/2	page 257
ADS 50/5	259
ADS_E 50/5	260
EPOS 24/5	271
MIP 10	273
Notes	**17**

Encoder MR
256 - 1024 CPT,
3 channels
Details page 239

Encoder HEDS 5540
500 CPT,
3 channels
Details page 243

Encoder HEDL 5540
500 CPT,
3 channels
Details page 245

Encoder HEDL 5540, 500 Counts per turn, 3 Channels, with Line Driver RS 422

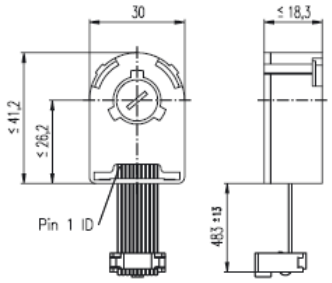

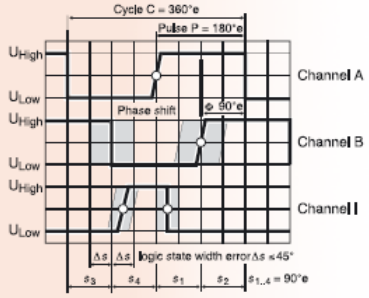

Stock program
Standard program
Special program (on request!)

Order Number	110512	110514	110516	110518
Type				
Counts per turn	500	500	500	500
Number of channels	3	3	3	3
Max. operating frequency (kHz)	100	100	100	100
Shaft diameter (mm)	3	4	6	8

Combination

+ Motor	Page	+ Gearhead	Page	+ Brake	Page	Overall length [mm] / ● see: + Gearhead			
RE 25, 10 W*	77					75.3			
RE 25, 10 W*	77	GP 26, 0.5 - 2.0 Nm	216			●			
RE 25, 10 W*	77	GP 32, 0.75 - 6.0 Nm	218/220			●			
RE 25, 10 W*	77	GP 32, 0.4 - 2.0 Nm	222			●			
RE 25, 20 W*	78					75.3			
RE 25, 20 W*	78	GP 26, 0.5 - 2.0 Nm	216			●			
RE 25, 20 W*	78	GP 32, 0.75 - 6.0 Nm	218/220			●			
RE 25, 20 W*	78	GP 32, 0.4 - 2.0 Nm	222			●			
RE 26, 18 W*	79					77.2			
RE 26, 18 W*	79	GP 26, 0.5 - 2.0 Nm	216			●			
RE 26, 18 W*	79	GP 32, 0.75 - 6.0 Nm	218/220			●			
RE 26, 18 W*	79	GP 32, 0.4 - 2.0 Nm	222			●			
RE 35, 90 W*	81						91.9		
RE 35, 90 W*	81	GP 32, 0.75 - 6.0 Nm	219/220				●		
RE 35, 90 W*	81	GP 42, 3.0 - 15 Nm	224				●		
RE 35, 90 W*	81			AB 40	279	124.1			
RE 35, 90 W*	81	GP 32, 0.75 - 6.0 Nm	219/220	AB 40	279	●			
RE 35, 90 W*	81	GP 42, 3.0 - 15 Nm	224	AB 40	279	●			
RE 36, 70 W*	82						92.2		
RE 36, 70 W*	82	GP 32, 0.75 - 6.0 Nm	219/220				●		
RE 36, 70 W*	82	GP 32, 0.4 - 2.0 Nm	222				●		
RE 36, 70 W*	82	GP 42, 3.0 - 15 Nm	224				●		
RE 40, 150 W*	83						91.7		
RE 40, 150 W*	83	GP 42, 3.0 - 15 Nm	224				●		
RE 40, 150 W*	83	GP 52, 4.0 - 30 Nm	227				●		
RE 40, 150 W*	83			AB 40	279	124.2			
RE 40, 150 W*	83	GP 42, 3.0 - 15 Nm	224	AB 40	279	●			
RE 40, 150 W*	83	GP 42, 4.0 - 30 Nm	227	AB 40	279	●			
RE 75, 250 W	84								241.5
RE 75, 250 W	84	GP 81, 20 - 120 Nm	230						●
RE 75, 250 W	84			AB 75	282				281.4
RE 75, 250 W	84	GP 81, 20 - 120 Nm	230	AB 75	282				●

*Pin allocation see page 245

Technical Data

Supply voltage	5 V ± 10 %
Output signal	EIA Standard RS 422
drivers used:	DS26LS31
Phase shift Φ (nominal)	90°e
Logic state width s	min. 45°e
Signal rise time (typical at C_L = 25 pF, R_L = 2.7 kΩ, 25°C)	180 ns
Signal fall time (typical at C_L = 25 pF, R_L = 2.7 kΩ, 25°C)	40 ns
Index pulse width (nominal)	90°e
Operating temperature range	0 ... +70°C
Moment of inertia of code wheel	≤ 0.6 gcm²
Max. angular acceleration	250 000 rad s^{-2}
Output current per channel	min. -20 mA, max. 20 mA
Option	1000 counts per turn, 2 channel

Pin Allocation for motor RE 75

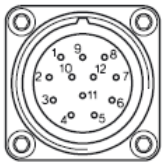

Flanged connector
Type SOURIAU 8GM-QL2-12P
1 V_{CC}
2 N.C. (do not connect)
3 GND
4 N.C. (do not connect)
5 Channel I (Index)
6 Channel $\overline{I}$
7 Channel B
8 Channel $\overline{B}$
9 Channel A
10 Channel $\overline{A}$
11 N.C. (do not connect)
12 N.C. (do not connect)
recommended cable plug
Type SOURIAU 8GM-DM2-12S (metal, straight exit:
maxon Art. No. 2675.538) or
8G-V2-12S (plastic, 90° angle:
maxon Art. No. 2675.539)

Connection example

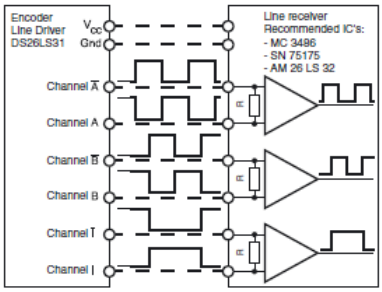

Terminal resistance R = typical 100 Ω

The slip-ring employed in this setup is a S10 model of *Michigan Scientific Inc.* Its spec sheet is shown in the following.

S Series Slip Ring Assembly

Models S4, S6, S8, S10

- 4,6,8 and 10 circuit slip rings
- Sealed against dust
- Color coded terminals
- Lightweight and compact
- Permanently lubricated bearings
- Rugged stainless steel construction
- Instrumentation quality rings and brushes

Description

Michigan Scientific's *S Series Slip Ring Assemblies* are utilized for a variety of applications requiring up to 10 circuit connections. They are designed to mount on the end of a rotating shaft and make electrical connection to strain gages, thermocouples, or other sensors that have been installed on rotating equipment. The slip ring brushes and rings are made of precious metals, which minimize noise and enable the assemblies to be used for low level instrumentation signals. In addition, a high grade stainless steel case provides protection from dust and other contaminants.

These *S Series* models are available in 4, 6, 8, and 10 circuit slip ring assemblies. Connections are made through color coded solder terminals located on both the slip ring rotor and slip ring stator. Permanently lubricated bearings eliminate the need for routine cleaning and maintenance. The lightweight and compact design of these slip ring assemblies make them ideal for use in applications where space is limited.

Specifications

	S4	S6	S8	S10
Circuits	4	6	8	10
Current Capacity per Circuit	500 mA	500 mA	500 mA	500 mA
Temperature Range*	-40°F to 250°F (-40°C to 121°C)	-40°F to 250°F (-40°C to 121°C)	-40°F to 250°F (-40°C to 121°C)	-40°F to 250°F (-40°C to 121°C)
RPM Rating	12,000	12,000	12,000	12,000
Maximum Peak Noise**	0.1Ω	0.1Ω	0.1Ω	0.1Ω
Weight	3.9 oz. (111 g)	4.0 oz. (113 g)	4.1 oz. (116 g)	4.2 oz. (119 g)
Length "A" (see back)	1.3 in (33 mm)	1.4 in (36 mm)	1.6 in (41 mm)	1.6 in (41 mm)
*For operation below 0°F, specify low temperature lubricant.				
** Resistance variation across slip ring contact				

S-Series Configuration

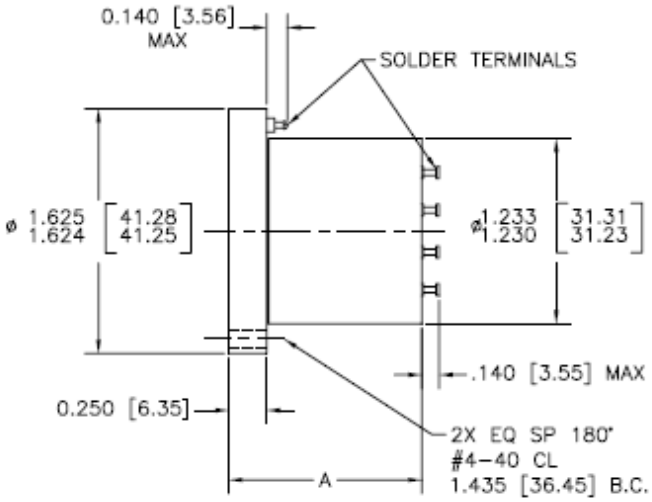

MODEL	A
S4	1.2 [30]
S6	1.3 [33]
S8	1.5 [38]
S10	1.5 [38]

The energy harvester itself consists of a cantilever beam which is a cut of the spring steel sheet for the PZT harvester and aluminium for the PVDF harvester. The mechanical properties of the substructure presented in chapter 5. Also mechanical and geometrical parameters of piezoelectric materials used presented in chapter 5. The piezoelectric materials are bonded to the substructure using sensor adhesives. A tip mass which is a cut of the large cube of steel, is weighed and attached to the tip of the beam for both PVDF and PZT harvesters. PVDF harvester tested with different masses. For this reason, we made holes on the beam to be able to screw the tip mass to the beam instead of using adhesive for connecting the mass to the beam.

BIBLIOGRAPHY

[1] Wang, W., Ismail, F. and Golnaraghi, F., “A Neuro-fuzzy Approach to Gear System Monitoring” *IEEE Transactions on Fuzzy Systems*, 2004, 12:710-723.

[2] Paradiso, J., and Starner, T., "Energy Scavenging for Mobile and Wireless Electronics", *IEEE Pervasive Computing*, 2005, Volume 4(1), pp. 18-27.

[3] Roundy, S., Wright, P. and Rabaey, J., “A Study of Low Level Vibrations as a Power Source for Wireless Sensor Nodes” *Computer Communications*, 2003, 26:1131-1144.

[4] Stark, I. and Stordeur, M., “New micro thermoelectric devices based on bismuth telluride-type thin solid films,” 18th International Conference on Thermo-electrics (ICT’99), Baltimore, MD, USA, 1999, IEEE, Piscataway, NJ USA, pp. 465–472.

[5] Lim, J., Snyder, G., Huang, C. K., Herman, J., Ryan, M., and Fleurial, J. P., “Thermoelectric microdevice fabrication process and evaluation at the Jet Propulsion Laboratory (JPL),” Thermoelectrics Proceedings ICT ’02. Twenty-First International Conference, Long Beach, CA, USA, 2002, pp. 535–539.

[6] Snyder, G., Lim, J., Huang, C. K., and Fleurial, J. P., “Thermoelectric microdevice fabricated by a MEMS-like electrochemical process,” Nature Materials, 2003, Vol. 2, No. 8, pp. 528–31.

[7] Strasser, M., Aigner, R., Lauterbach, C., Sturm, T., Franosch, M., and Wachutka, G., “Micromachined cmos thermoelectric generators as on-chip power supply,” TRANSDUCERS, Solid-State Sensors, Actuators and Microsystems, 12th International Conference, Boston, MA, USA, 2003, Vol. 1, pp. 45–48.

[8] Holmes, A., Hong, G., Pullen, K., and Buffard, K., “Axial-flow mircoturbine with electromagnetic generator: design, CFD simulation, and prototype demonstration.” 17th International IEEE Micro Electro Mechanical Conference, Maastricht Netherlands, 2004, IEEE, Piscataway, NJ USA, pp. 568 – 571.

[9] Jansen, A. J. and Stevels, A. L. N. “Human Power, a Sustainable Option for Electronics,” *Proc. of IEEE Int. Symposium on Electronics and the Environment*, 1999, pp. 215-218.

[10] Donelan, J. M., Li, Q. and Naing, V., “Biomechanical energy harvesting: Generating electricity during walking with minimal user effort” *Science*, 2008, 319(5864): 807–810.

[11] Mitcheson, P., Stark, B., Miao, P., Yeatman, E., Holmes, A., and Green, T., “Analysis and optimisation of MEMS electrostatic on-chip power supply for self-powering of slow-sensors,” Eurosensors, Portugal, 2003, pp. 48–51.

[12] Williams, C.B. and Yates, R.B., “Analysis of a Micro-electric Generator for Microsystems” *Sensors and Actuators A*, 1996, 52:8-11.

[13] Meninger, S., Mur-Miranda, J., Lang, J., Chandrakasan, A., Slocum, A., Schmidt, M. and Amirtharajah, R., “Vibration to electric energy conversion” *IEEE Trans Very Large Scale Integration (VLSI) Syst.,* 2001, (9) 64–76.

[14] Sterken, T., Fiorini, P., Baert, K., Puers, R. and Borghs, G., “An Electret-based Electrostatic Micro Generator” *TRANSDUCERS, Solid-State Sensors, Actuators and* Microsystems, 12th International Conference, Boston, MA, USA, 2003, 1291 – 1294.

[15] Beeby, S.P., Tudor, M.J. and White, N.M., “Energy Harvesting Vibration Sources for Microsystems Applications” *Meas. Sci. Technol.,* 2006, 17 175-195.

[16] El-Hami, M., Glynne-Jones, P., James, E., Beeby, S. P., White, N. M., Brown, A. D., Ross, J. N. and Hill, M., “Design and fabrication of a new vibration-based electromechanical power generator” *Sensors Actuators* A., 2001, (92) 335–42.

[17] Anton, S. and Sodano, H., “A Review of Power Harvesting Using Piezoelectric Materials (2003-2006),” *Smart Materials and Structures,* 2007, (16) 1-21.

[18] Yang, B., Lee, C., Kee, W. L. and Lim, S. P., “Hybrid energy harvester based on piezoelectric and electromagnetic mechanisms”, *J. Micro/Nanolith, MEMS MOEMS,* 2010, 9, 023002, p. 1-10.

[19] Curie, J. and Curie, P., C. R. Acad Sci. Paris, 1880.

[20] Ikeda, T., Fundamentals of Piezoelectricity, Oxford University Press, New York, 1996.

[21] Jaffe, B., Cook,W. R., and Jaffe, H., Piezoelectric Ceramics, R.A.N. Publishers, Marietta, OH, 1971.

[22] Parker, M., Ambient Energy Harvesting, Master’s Thesis, The University of Queensland, Australia, October 2003.

[23] Carazo, A. V., “Novel piezoelectric transducers for high voltage measurements”, PhD thesis, Universitat Politecnica de Catalunya, Barcelona, January 2000.

[24] Repas, R., Piezoelectric Force Sensors, Sensor Sense, February 2008.

[25] Heywang, W., Lubitz, K. And Wersing, W., Piezoelectricity: Evolution and Future of a Technology, Springer Series in Materials Science, 2008.

[26] Kawai, H., “The Piezoelectricity of Poly Vinylidene Fluoride” *Japanese Journal of Applied Physics,*1969, Vol. 8, Issue 7, pp.975.

[27] Hausler, E. and Stein, E., “Implantable Physiological Power Supply with PVDF Film,” *Ferroelectrics*, 1984, Vol. 60, 277-282.

[28] Schmidt, V. H., “Piezoelectric Energy Conversion in Windmills,” *Ultrasonics Symposium*, 1992, vol. 2, pp. 897-904.

[29] Starner, T. “Human-powered Wearable Computing,” *IBM Systems Journal*, 1996, Vol. 36, Nos. 3 & 4, pp. 618-629.

[30] Umeda, M, Nakamura, K. and Ueha, S. “Analysis of the Transformation of Mechanical Impact Energy to Electric Energy Using Piezoelectric Vibrator,” *Japan Journal of Applied Physics*, 1996, Volume 35, Part 1, No. 5B, pp. 3267-3273.

[31] Umeda, M., Nakamura, K. and Ueha, S. “Energy Storage Characteristics of a Piezo-generator Using Impact Vibration,” *Japan Journal of Applied Physics,* 1997, Vol. 36, Part 1, No. 5B, pp. 3146-3151.

[32] Kymissis, J., Kendall, C., Paradiso, J. and Gershenfeld, N., “Parasitic Power Harvesting in Shoes,” *Proceedings of the Second IEEE International Conference on Wearable Computing, (ISWC)*, Pittsburgh, Pennsylvania, USA, 1998, IEEE Computer Society Press, pp. 132-139.

[33] Kimura, M, “Piezoelectric Generation Device,” US Patent, 1998, Number 5,801,475.

[34] Goldfarb, M. and Lowell, D.J. “On the Efficiency of Electric Power Generation with Piezoelectric Ceramic,” *Journal of Dynamic Systems, Measurement, and Control*, 1999, Vol. 121, pp. 566-571.

[35] Allen, J. and Smits, A. “Energy Harvesting Eel,” *Journal of Fluids and Structures*, 2001, Vol. 15, pp. 629-40.

[36] Ramsay, M. J. and Clark, W. W. “Piezoelectric Energy Harvesting for Bio MEMS Applications,” *Proceedings of the SPIE 8th Annual Smart Materials and Structures Conference*, Newport Beach, CA, 2001, Vol. 4332, pp. 429-438.

[37] Elvin, N. G., Elvin, A. A. and Spector, M. “A Self-powered Mechanical Strain Energy Sensor,” *Smart Materials and Structures*, 2001, Vol. 10, pp. 293-299.

[38] Ottman, G.K., Hofmann, H.F. and Lesieutre, G.A., “Optimized piezoelectric energy harvesting circuit using step-down converter in discontinuous conduction mode” *Proc. of IEEE’s 33rd Annual Power Electronics Specialists Conf.,* 2002, *Cairns, Queensland, Australia,* 4 1988-94.

[39] Sodano, H. A., Park, G., Leo, D. J. and Inman, D. J. “Use of piezoelectric energy harvesting devices for charging batteries” Proceedings of SPIE, 2003, Vol. 5050, pp. 101 – 108.

[40] Sodano, H. A., Inman, D. J. and Park, G. “A review of power harvesting from vibration using piezoelectric materials” *The Shock and Vibration Digest*, 2004, Vol. 36, No. 3, 197-205.

[41] Granstrom, J., Feenstra, J., Sodano, H. A. and Farinholt, K. “Energy harvesting from a backpack instrumented with piezoelectric shoulder straps” *Smart Materials and Structures,* 2007, (16) 1810-1820.

[42] Khameneifar, F. and Arzanpour, S., “Energy harvesting from pneumatic tires using piezoelectric transducers” *SMASIS 2008* Smart Materials, Adaptive Structures and Intelligent Systems, Ellicott City, Maryland, USA, 2008, 331-337.

[43] Ertuk, A., Renno, J. M. and Inman, D. J., “Modeling of piezoelectric energy harvesting from an L-shaped beam-mass structure with an application to UAVs” *Intelligent Mate. Sys. Struct.,* 2009, Vol. 20, No. 5, 529-544.

[44] Khameneifar, F., Arzanpour, S. and Moallem, M. “Vibration energy harvesting from a hydraulic engine mount via PZT decoupler”, ASME International Mechanical Engineering Congress and Exposition, Vancouver, BC, Canada, 2010, pp. 1-8.

[45] Priya, S. and Inman, D. J., “Energy harvesting technologies”, Springer, 2009, 524 p.

[46] duToit, N. E., Wardle, B. L. and Kim, S.G., “Design considerations for MEMS-scale piezoelectric mechanical vibration energy harvesters”, *Integr. Ferroelectr.,* 2005, (71) 121–60.

[47] Erturk, A. and Inman, D. J., “Issues in mathematical modelling of piezoelectric energy harvesters” *Smart Mater. Struct.,* 2008, 17, No. 6, 14p.

[48] Erturk, A. and Inman, D. J., “On mechanical modeling of cantilevered piezoelectric vibration energy harvesters” *J. Intell. Mater. Syst. Struct.,* 2008, (19) 1311–25.

[49] Sodano, H. A., Park, G. and Inman, D. J., “Estimation of electric charge output for piezoelectric energy harvesting” *Strain,* 2004, (40) 49–58.

[50] Erturk, A. and Inman, D. J., “An Experimentally Validated Bimorph Cantilever Model for Piezoelectric Energy Harvesting from Base Excitations” *Smart Materials and Structures*, 2009, 18:025009:1-18.

[51] Wang, Q. M. and Cross, L. E., “Constitutive equations of symmetrical triple layer piezoelectric benders” *IEEE Trans. Ultrason. Ferroelectr. Freq. Control,* 1999, (46) 1343–51.

[52] Kermani, M. R., Moallem, M. and Patel, R. V., “Parameter Selection and Control Design for Vibration Suppression Using Piezoelectric Transducers” *Control Engineering Practice*, 2004, 12:1005–1015.

[53] Ottman, G. K., Hofmann, H. F., Bhatt, A. C. and Lesieutre, G. A., “Adaptive Piezoelectric Energy Harvesting Circuit for Wireless Remote Power Supply” *IEEE Transactions on Power Electronics,* 2002, 17(5):669-676.

[54] Renno, J. M., Daqaq, M. F. and Inman, D. J., “On the optimal energy harvesting from a vibration source” *Journal of Sound and Vibration,* 2009, Vol. 320, 386-405.

[55] http://www.sensorsportal.com/HTML/SENSORS/Wireless_Sens_Manuf.htm

[56] Shen, D., Choe, S.Y. and Kim, D.J., “Comparison of Piezoelectric Materials for Vibration Energy Conversion Devices” *Mater. Res. Soc. Symp. Proc.,* 2007, 966:1-6.

[57] Inman, D. J., *Engineering Vibration,* 3rd edition, Prentice Hall, 2008.

[58] Harris, C. M., *Shock and Vibration Handbook*, McGraw-Hill, New York, 1987.